Supplementary Information for

Photothermal-promoted anion exchange membrane seawater electrolysis on a nickel-molybdenum-based catalyst

Libo Wu[1,2], Wanheng Lu[1], Wei Li Ong[1], Andrew See Weng Wong[3], Yuanming Zhang[1], Tianxi Zhang[1], Kaiyang Zeng[4], Zhifeng Ren[5]*, Ghim Wei Ho[1,2,6]*

[1]Department of Electrical and Computer Engineering, National University of Singapore, Singapore 117581, Singapore

[2]Centre for Hydrogen Innovations, National University of Singapore, Singapore, 117580, Singapore

[3]Facility for Analysis Characterization Testing and Simulation (FACTS), Nanyang Technological University, Singapore 639798, Singapore

[4]Department of Mechanical Engineering, National University of Singapore, Singapore 117576, Singapore

[5]Department of Physics and Texas Center for Superconductivity at the University of Houston (TcSUH), University of Houston, Houston, TX 77204, USA

[6]Department of Materials Science and Engineering, National University of Singapore, Singapore 117575, Singapore

* Email: zren@uh.edu; elehgw@nus.edu.sg

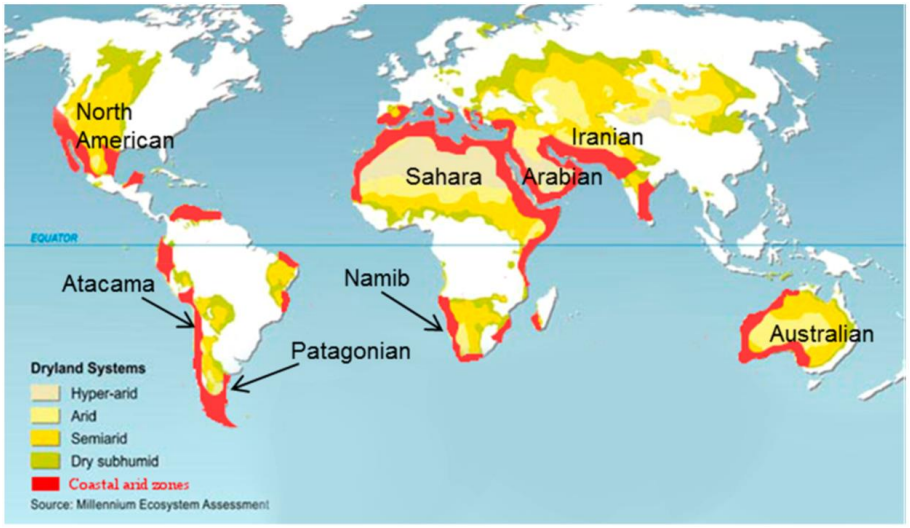

Supplementary Fig. S1. Dryland areas of the earth with coastal arid zones highlighted in red. Reprinted with permission from ref 1.(*1*) Copyright 2019 American Chemical Society. Data source: Ecosystems and human Well-being. World Resources Institute, 2005.(*2*)

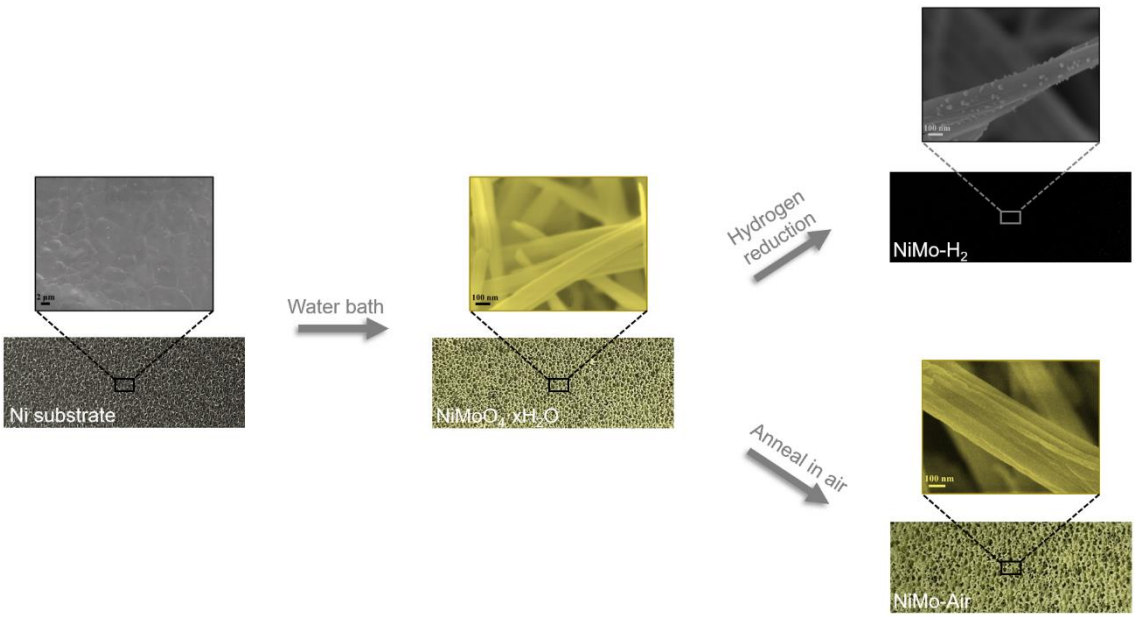

Supplementary Fig. S2. Synthesis routines and photographs and SEM images of Ni substrate, $NiMoO_4 \cdot xH_2O$, NiMo-H_2, and NiMo-Air samples.

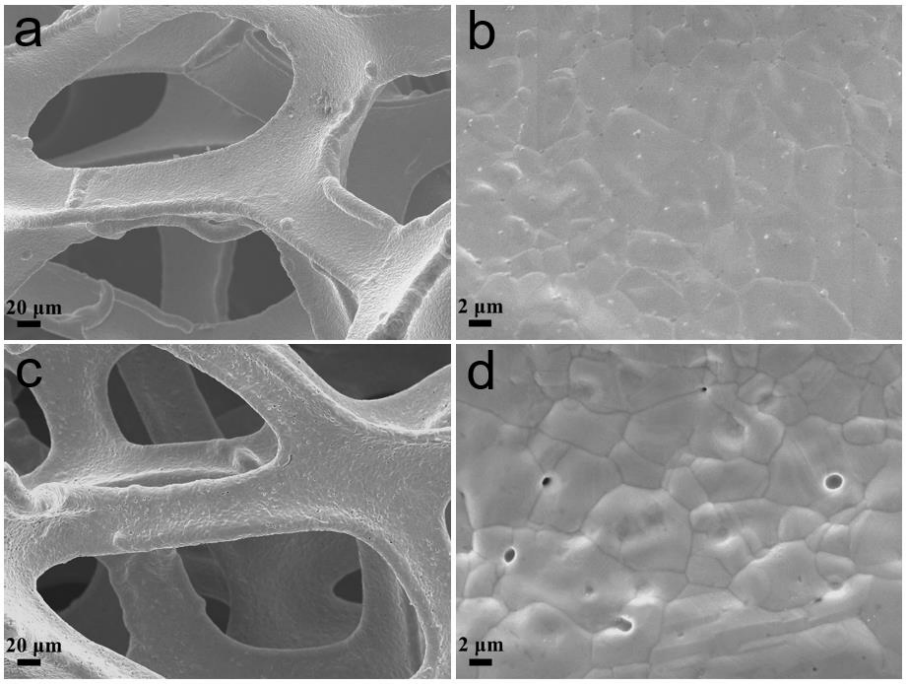

Supplementary Fig. S3. SEM images of hollow (a-b) nickel foam and (c-d) copper foam substrates.

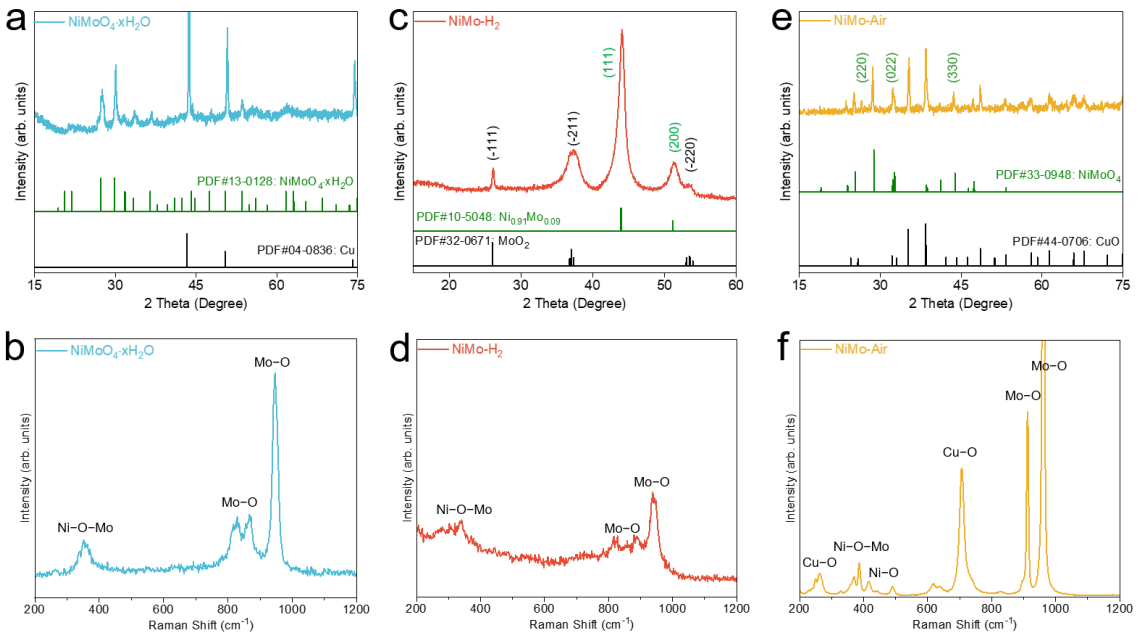

Supplementary Fig. S4. XRD patterns (top) and Raman spectra (bottom) for (a-b) $NiMoO_4 \cdot xH_2O$, (c-d) NiMo-H_2, and (e-f) NiMo-Air samples. To avoid the potential interference from nickel foam substrate, all XRD measurements reported were performed using samples grown on or peeled off from copper foam substrate.

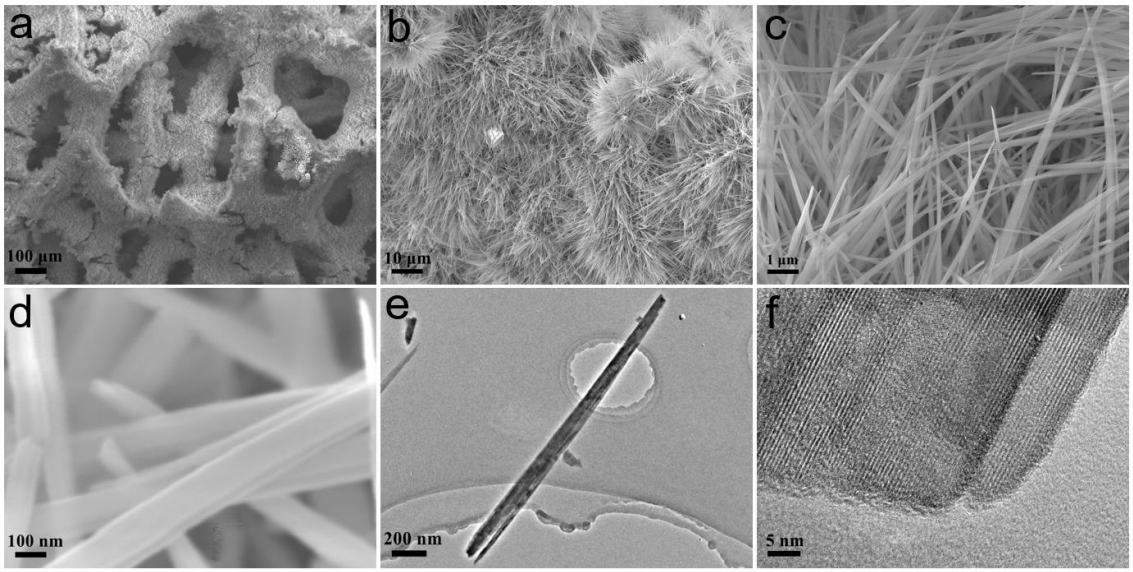

Supplementary Fig. S5. (a-d) SEM, (e) TEM, and (f) HRTEM images of the $NiMoO_4 \cdot xH_2O$ precursor.

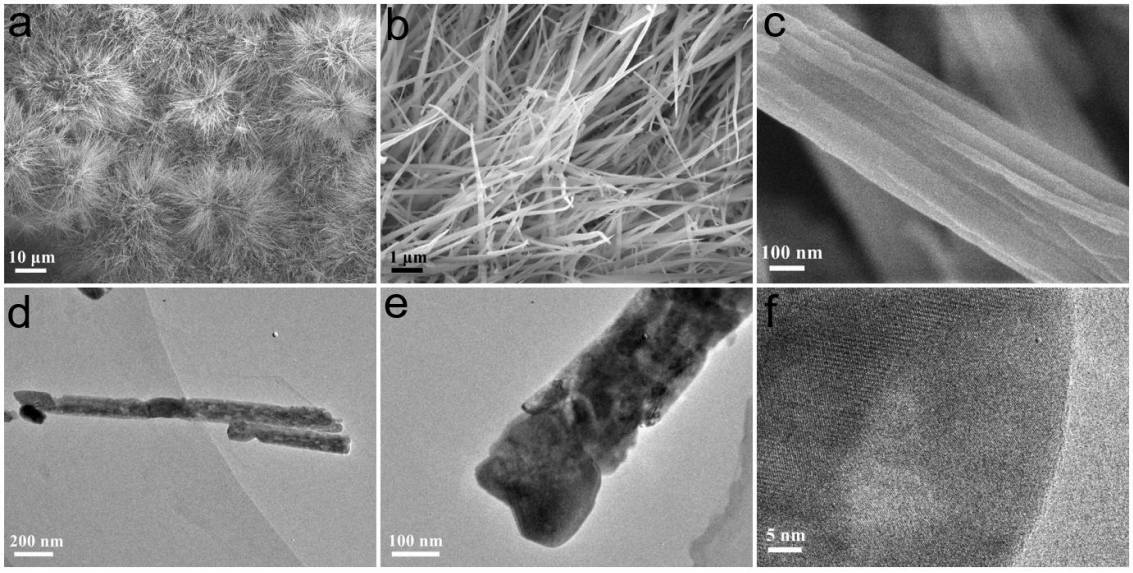

Supplementary Fig. S6. (a-d) SEM, (e) TEM, and (f) HRTEM images of the NiMo-Air sample.

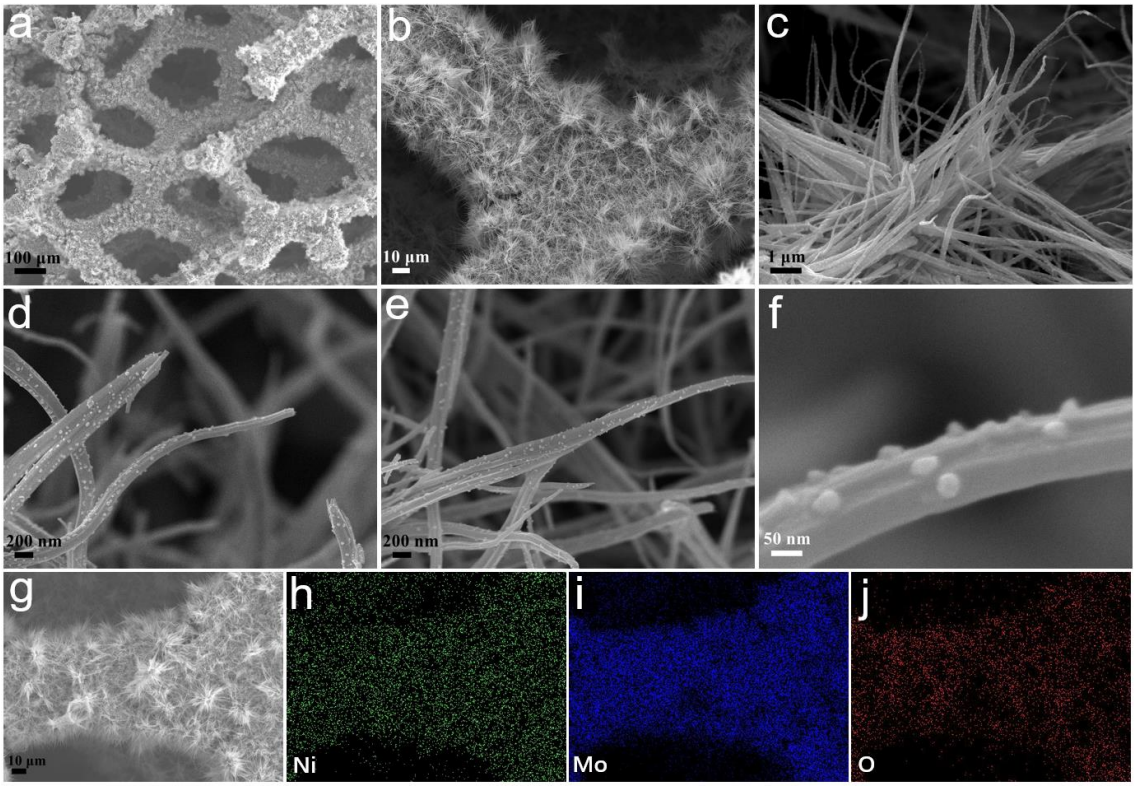

Supplementary Fig. S7. (a-g) SEM images of the NiMo-H_2 sample. (h) Ni, (i) Mo, and (j) O EDS mapping images corresponding to (g).

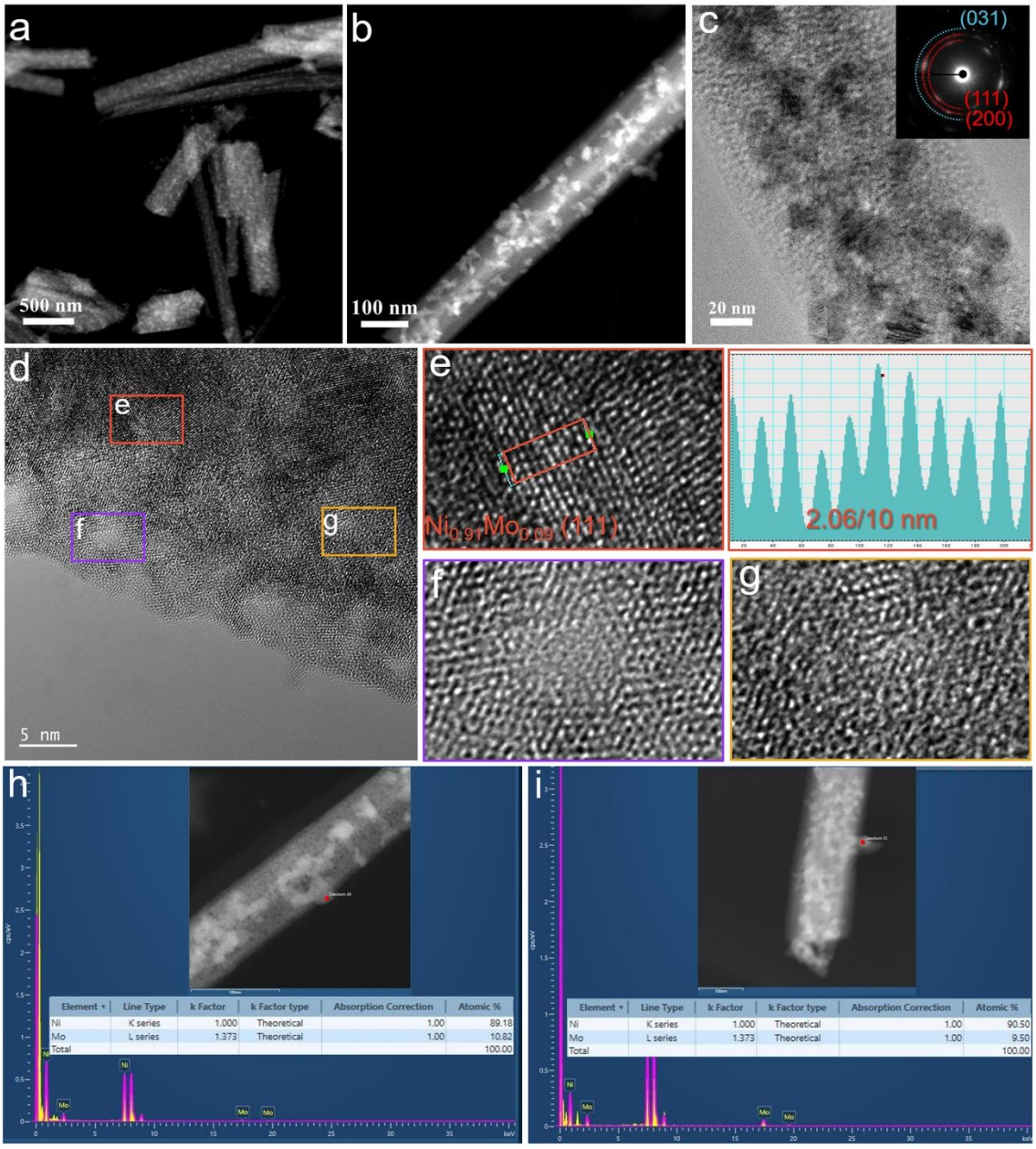

Supplementary Fig. S8. (a-c) TEM images and SAED pattern of the NiMo-H_2 sample. (d) Overview and (e-g) detailed HRTEM images of the NiMo-H_2 sample. (h) and (i) TEM EDS spectra of the Ni-Mo alloy nanoparticle inside the NiMo-H_2 sample.

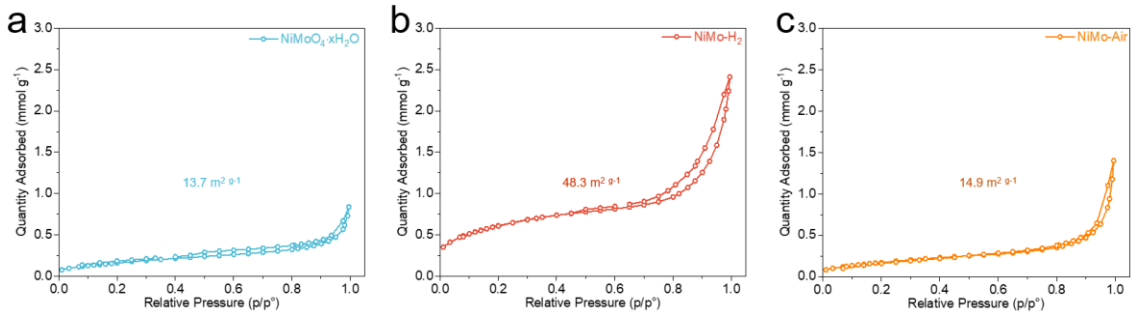

Supplementary Fig. S9. Nitrogen adsorption–desorption isotherms curves of the (a) $NiMoO_4 \cdot xH_2O$ precursor, (b) NiMo-H_2, and (c) NiMo-Air samples.

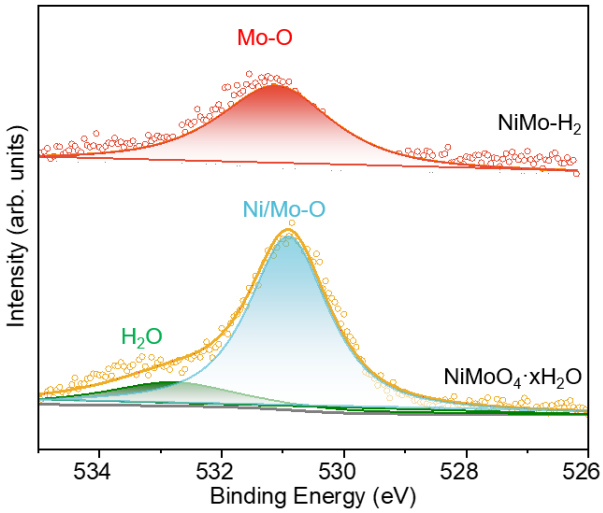

Supplementary Fig. S10. High-resolution XPS spectra of O for $NiMoO_4 \cdot xH_2O$ (bottom) and NiMo-H_2 (top) samples.

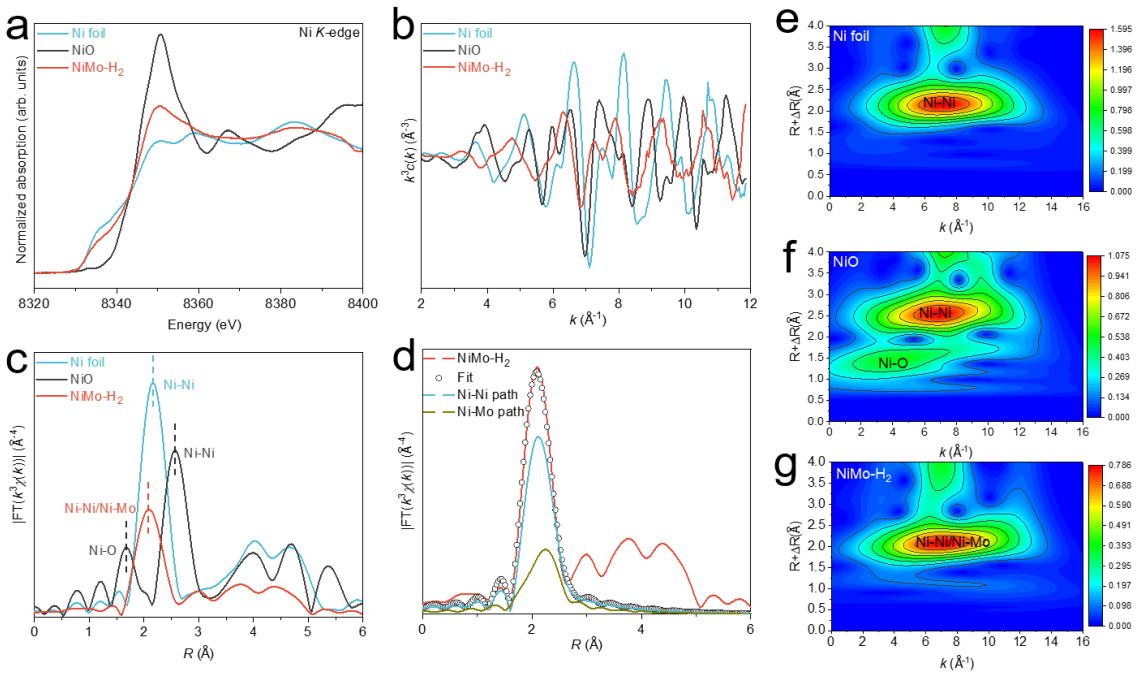

Supplementary Fig. S11. (a) Ni K-edge XANES spectra, (b) corresponding Ni K-edge oscillation curves and (c) Fourier-transformed Ni K-edge EXAFS spectra of the Ni foil, NiO, and NiMo-H_2 sample. (d) Fitting of the magnitude of the Fourier transform of the Ni K-edge EXAFS for NiMo-H_2 sample. Wavelet transforms of k^3-weighted EXAFS spectra of Ni K-edge for (e) Ni foil, (f) NiO, and (g) NiMo-H_2 sample.

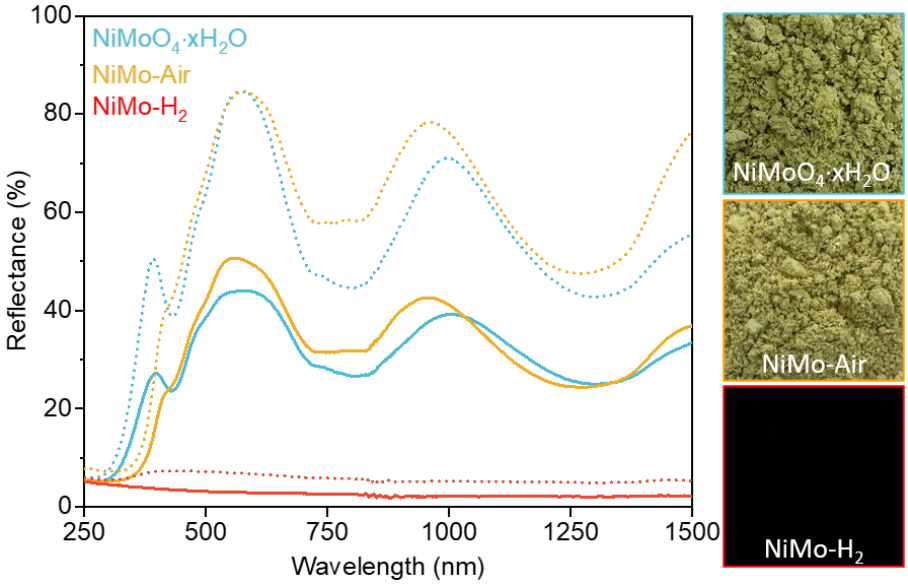

Supplementary Fig. S12. Left: UV–vis–NIR reflectance spectra for $NiMoO_4 \cdot xH_2O$, NiMo-Air, and NiMo-H_2 samples in their self-supported (solid lines) and powder (dashed lines) states. Right: photographs of the powdered samples.

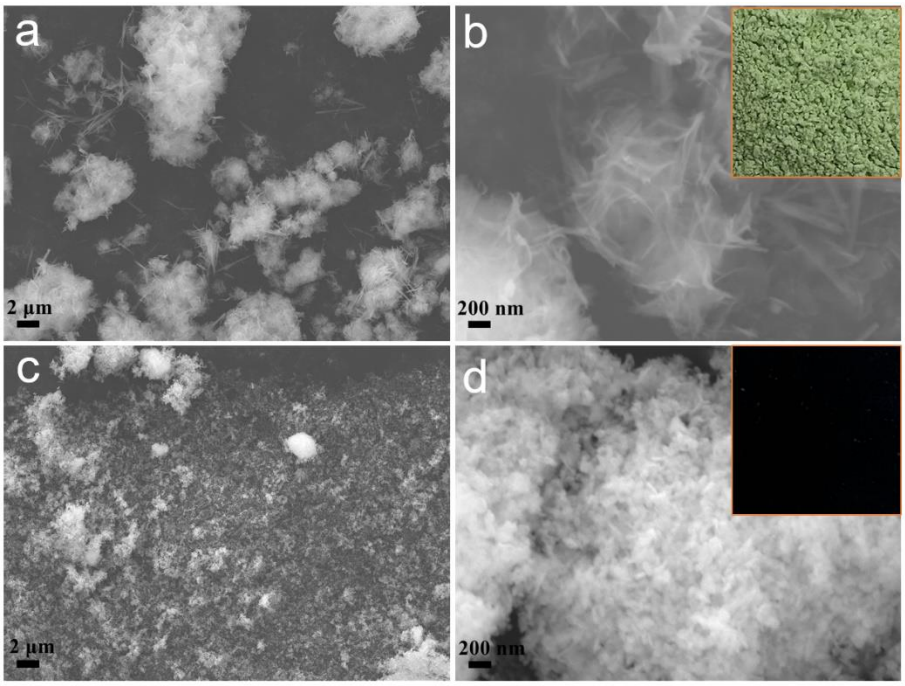

Supplementary Fig. S13. SEM images of (a-b) the Ni-Mo-O precursor and (c-d) Ni-Mo alloy nanoparticles. Insets to (b) and (d): photographs of the Ni-Mo-O precursor and Ni-Mo alloy nanoparticles, respectively.

To prepare powdered Ni-Mo nanoparticles, a Ni-Mo-O precursor was first prepared through a hydrothermal reaction. In detail, 6 mmol $Ni(NO_3)_2 \cdot 6H_2O$, 0.75 mmol $(NH_4)_6Mo_7O_{24} \cdot 4H_2O$, and 9 mmol $CO(NH_2)_2$ were homogeneously dissolved in 60 mL DI water in a 100 mL Teflon-lined stainless steel autoclave, which was then transferred to an oven maintained at 120 °C for 12 h. After the hydrothermal reaction, the precipitated Ni-Mo-O powder was collected, dried, and then reduced at 500 °C for 6 h under a mixed hydrogen-nitrogen flow to obtain Ni-Mo nanoparticles.

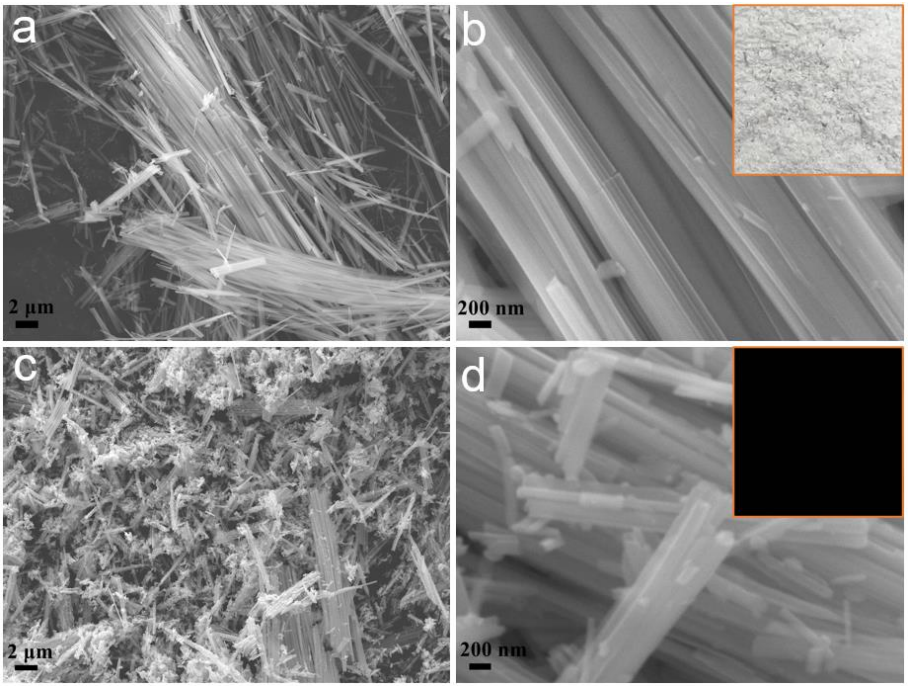

Supplementary Fig. S14. SEM images of (a-b) the Mo-O precursor and (c-d) MoO_2 nanorods. Insets to (b) and (d): photographs of the Mo-O precursor and MoO_2 nanorods, respectively.

To synthesize powdered MoO_2 nanorods, a Mo-O precursor was first prepared according to a previous report.(*3*) In detail, 1 mmol $(NH_4)_6Mo_7O_{24}\cdot 4H_2O$ was first dissolved in 90 mL DI water with stirring, followed by the addition of 0.9 mL ethylenediamine ($H_2NCH_2CH_2NH_2$, Sigma Aldrich). Subsequently, 1 M HCl was added dropwise into the solution until a white precipitate was formed. Afterward, the solution was heated at 50 °C for 3 h and the Mo-O precursor was collected by filtration and washing. MoO_2 nanorods were obtained through hydrogen reduction of the Mo-O precursor at 500 °C for 2 h.

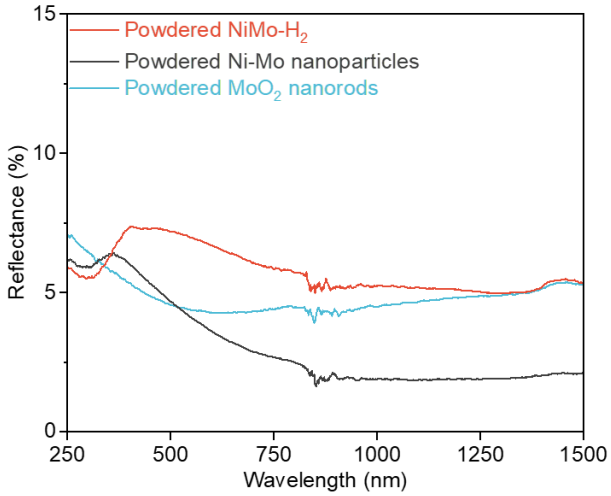

Supplementary Fig. S15. UV–vis–NIR reflectance spectra for powdered NiMo-H_2, Ni-Mo alloy nanoparticle, and MoO_2 nanorod samples.

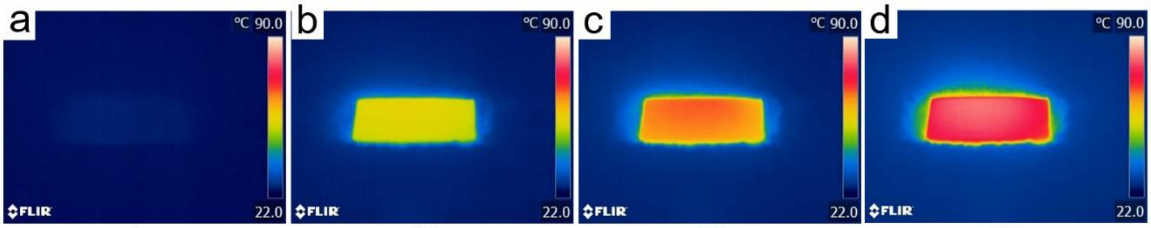

Supplementary Fig. S16. Infrared images of the NiMo-H_2 catalyst during exposure to simulated one sun irradiation for different amounts of time.

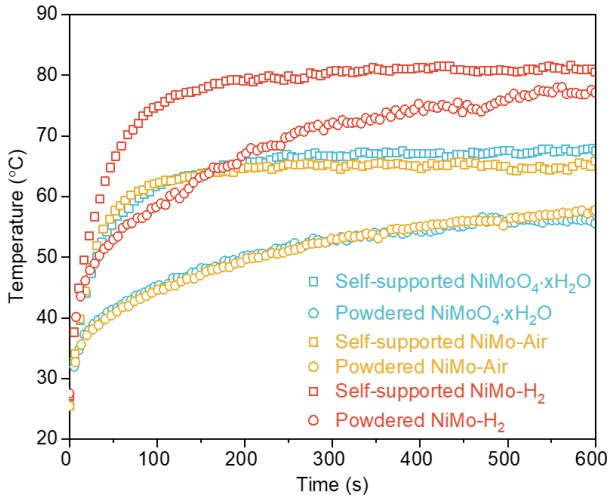

Supplementary Fig. S17. Temperature evolution curves for self-supported and powdered $NiMoO_4 \cdot xH_2O$, NiMo-Air, and NiMo-H_2 samples under simulated one sun irradiation.

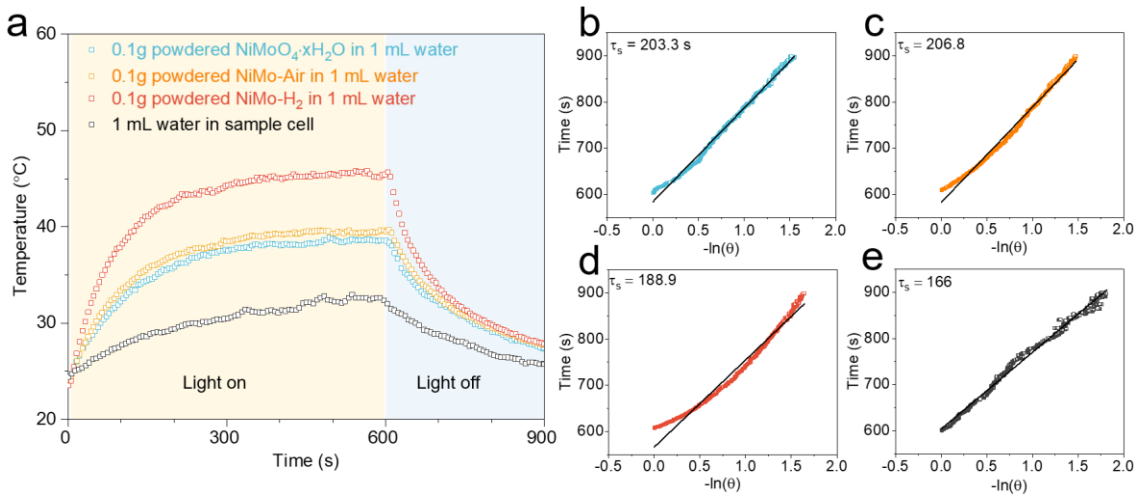

Supplementary Fig. S18. Temperature evolution curves under simulated one sun irradiation for the $NiMoO_4 \cdot xH_2O$, NiMo-Air, and NiMo-H_2 solutions as well as water in sample cell. The light was turned off after irradiation for 600 s. Plots of cooling time versus negative natural logarithm of the temperature driving force for the (b) $NiMoO_4 \cdot xH_2O$, (c) NiMo-Air, (d) NiMo-H_2 solution as well as (e) water obtained from the light off area.

To measure the photothermal conversion efficiency (η) of as-synthesized samples in water, solutions of $NiMoO_4 \cdot xH_2O$, NiMo-Air, and NiMo-H_2 were prepared by dispersing 0.1 g of each sample in 1 mL DI water. Each solution was put in a sample cell and exposed to one sun irradiation for 10 min, after which the light was turned off. The temperature evolution curves were recorded, and η was calculated through Equation 1:(*4-8*)

$$\eta = \frac{hA(T_{\max} - T_{\text{sur}}) - \mathrm{Q}_{\text{loss}}}{I(1 - 10^{-a_\lambda})} \quad (1)$$

where h is the heat transfer coefficient, A is the surface area of heat transfer (9.62 cm^2), T_{max} is the maximum equilibrium temperature, T_{sur} is the temperature of surrounding environment, Q_{loss} stands for the heat dissipation from the light absorbed by water and sample cell, I is the radiation intensity of the incident light (100 mW cm^{-2}), and a_λ represents the absorbance of the photothermal material at the wavelength λ. Since absorbance in the vis–NIR range is more effective for photothermal conversion, the average absorbance of the sample within the 400 to 1500 nm wavelength range is used here. The value of hA can be derived from Equation 2:(*5*)

$$\tau_s = \frac{m_{\mathrm{D}} C_{\mathrm{D}}}{hA} \quad (2)$$

and Q_{loss} can calculated through Equation 3:

$$Q_{loss} = \frac{(m_{\mathrm{D,water}} C_{\mathrm{D,water}} + m_{\mathrm{D,sample\ cell}} C_{\mathrm{D,sample\ cell}})(T_{\max} - T_{\mathrm{sur}})}{\tau_{\mathrm{s,water\ and\ sample\ cell}}} \quad (3)$$

where τ_s is the time constant for heat transfer of the system, m_D and C_D are the mass (1 g for DI water and 0.69 g for the bottom of the sample cell) and heat capacity (4.2 J g^{-1} for DI water and 1.3 J g^{-1} for sample cell) of the water and sample cell, respectively. Other parameters and equations involved are:(*8*)

$$\theta = \frac{T - T_{\mathrm{sur}}}{T_{\max} - T_{\mathrm{sur}}} \quad (4)$$

$$t = -\tau_s ln\theta \quad (5)$$

where θ is a dimensionless parameter and t is time (s). T_{max}, T_{sur} and corresponding τ_s for each sample can be obtained from the figure above. As a result, the photothermal conversion efficiency of each sample in water was calculated to $\eta_{NiMoO_4 \cdot xH_2O}$ = 19.5%, $\eta_{NiMo\text{-}Air}$ = 26.4%, and $\eta_{NiMo\text{-}H_2}$ = 42%, respectively.

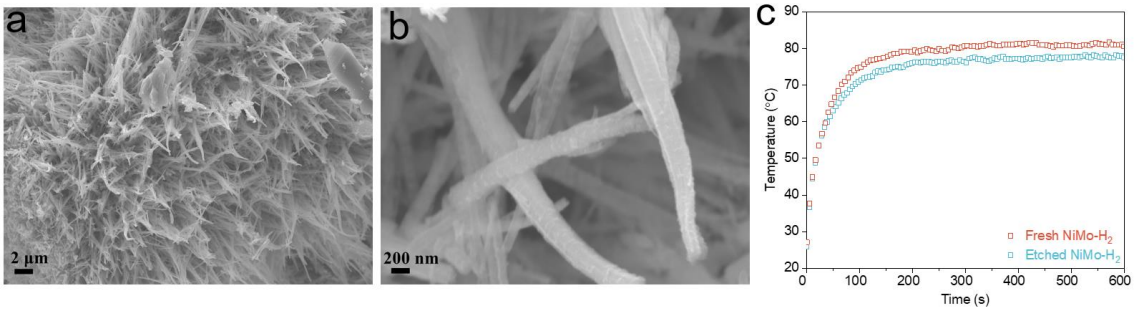

Supplementary Fig. S19. (a-b) SEM images of the etched NiMo-H_2 sample. (c) Temperature evolution curves for the fresh and etched NiMo-H_2 samples.

The etched NiMo-H_2 sample was prepared by immersing a fresh NiMo-H_2 sample in 0.5 M H_2SO_4 solution for 1 h to partially remove $Ni_{0.91}Mo_{0.09}$ nanoparticles from the MoO_2 nanorods.

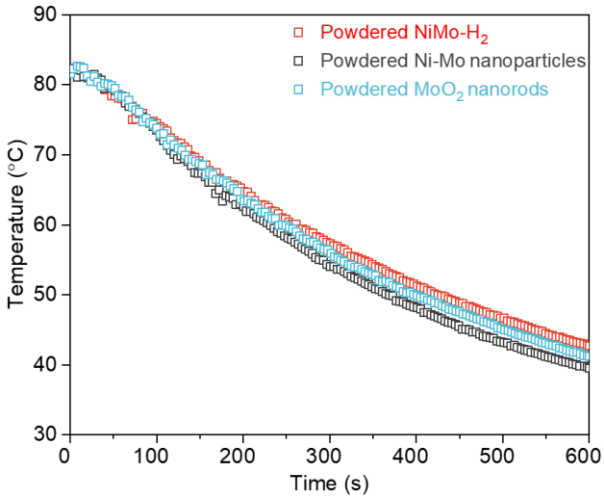

Supplementary Fig. S20. Heat retention ability tests for powdered NiMo-H_2, Ni-Mo alloy nanoparticle, and MoO_2 nanorod samples.

To measure the heat retention performance of these sample, equal masses of samples were first heated to ~82 °C and maintained for 30 min. Afterward, the heat source was removed, allowing the samples to cool down naturally, and the temperature change of these samples was measured using an infrared camera. After naturally cooling down for 10 min, the NiMo-H_2 sample exhibits the highest heat retention ability among these three samples, maintaining a temperature of ~42.7 °C. Notably, the MoO_2 sample retained a temperature of ~41.2 °C, which is ~1.7 °C higher than that of the Ni-Mo alloy sample (~39.5 °C), demonstrating a better heat retention ability.

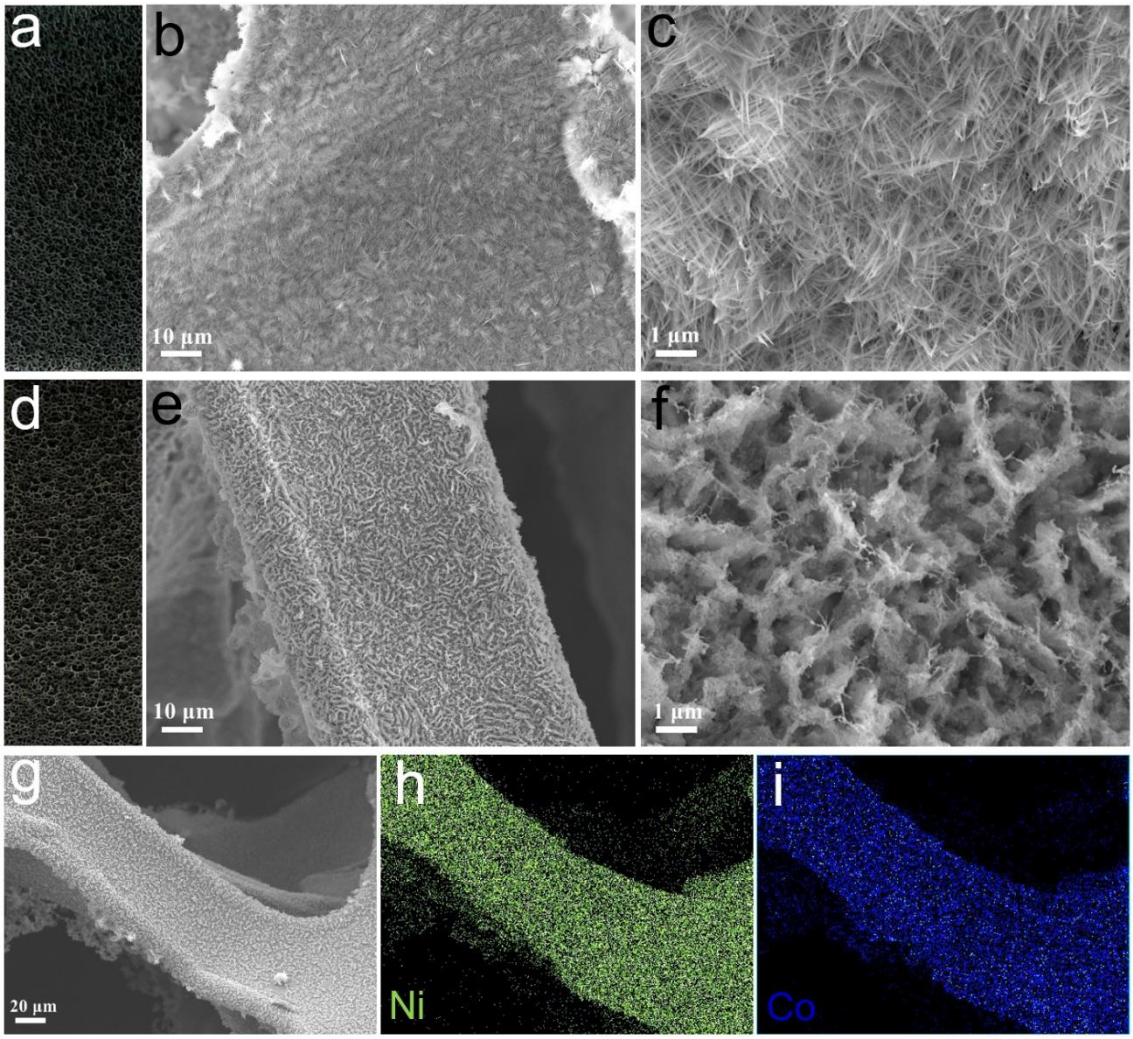

Supplementary Fig. S21. (a) Photograph and (b-c) SEM images of the NiCo LDH precursor. (d) Photograph and (e-g) SEM images of the NiCo-H_2 catalyst. (h) Ni and (i) Co EDS mapping images corresponding to (g).

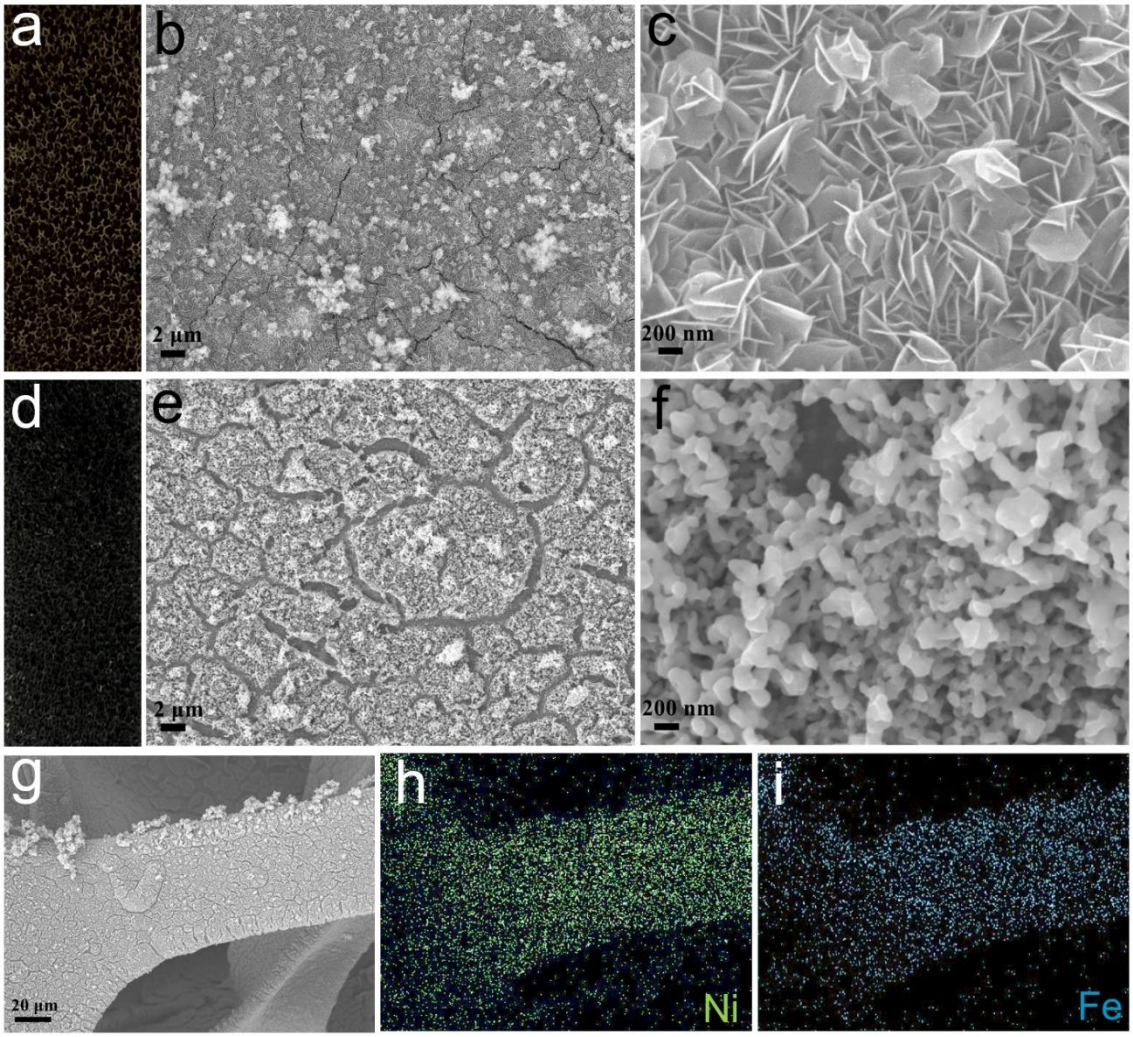

Supplementary Fig. S22. (a) Photograph and (b-c) SEM images of the NiFe LDH precursor. (d) Photograph and (e-g) SEM images of the NiFe-H_2 catalyst. (h) Ni and (i) Fe EDS mapping images corresponding to (g).

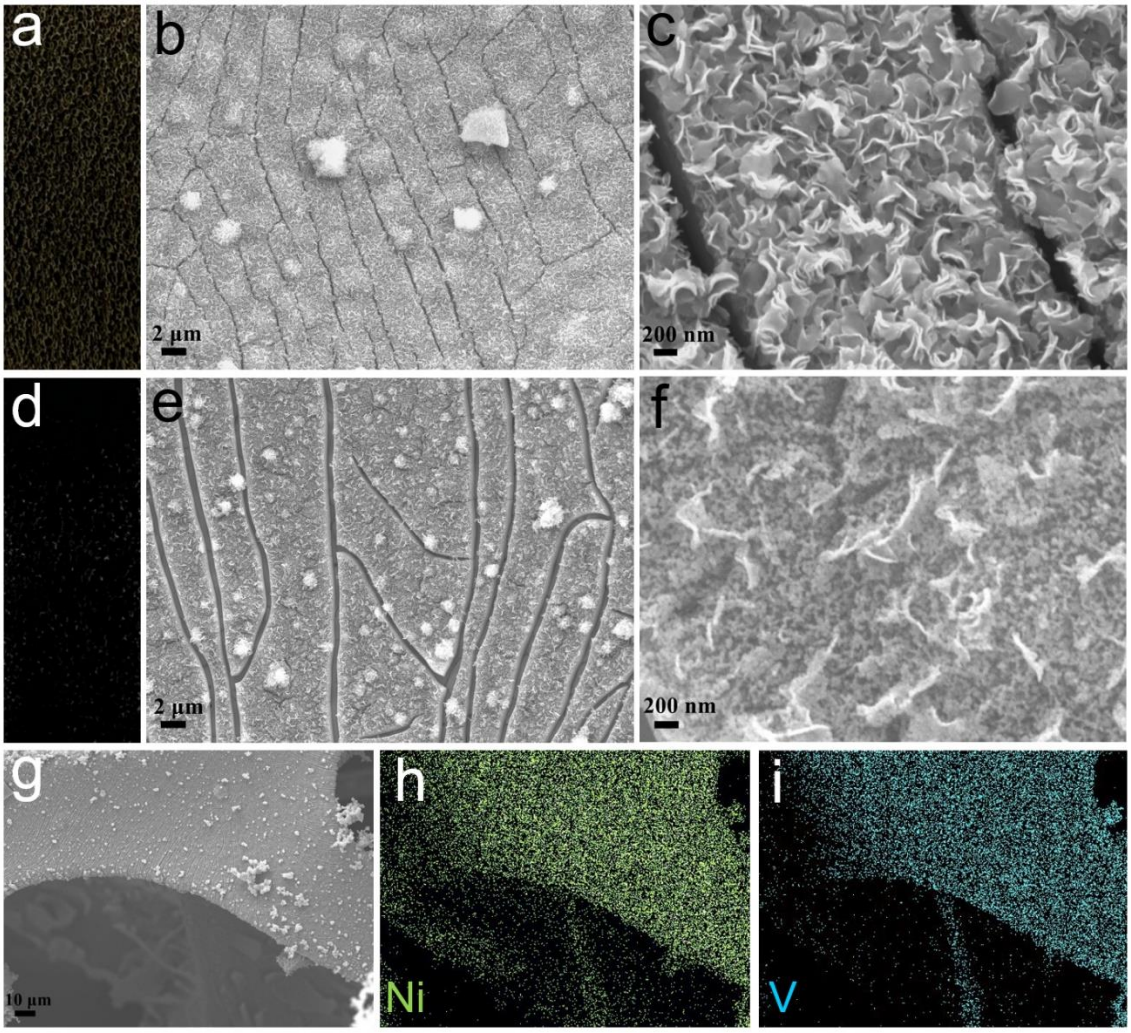

Supplementary Fig. S23. (a) Photograph and (b-c) SEM images of the NiV LDH precursor. (d) Photograph and (e-g) SEM images of the NiV-H_2 catalyst. (h) Ni and (i) V EDS mapping images corresponding to (g).

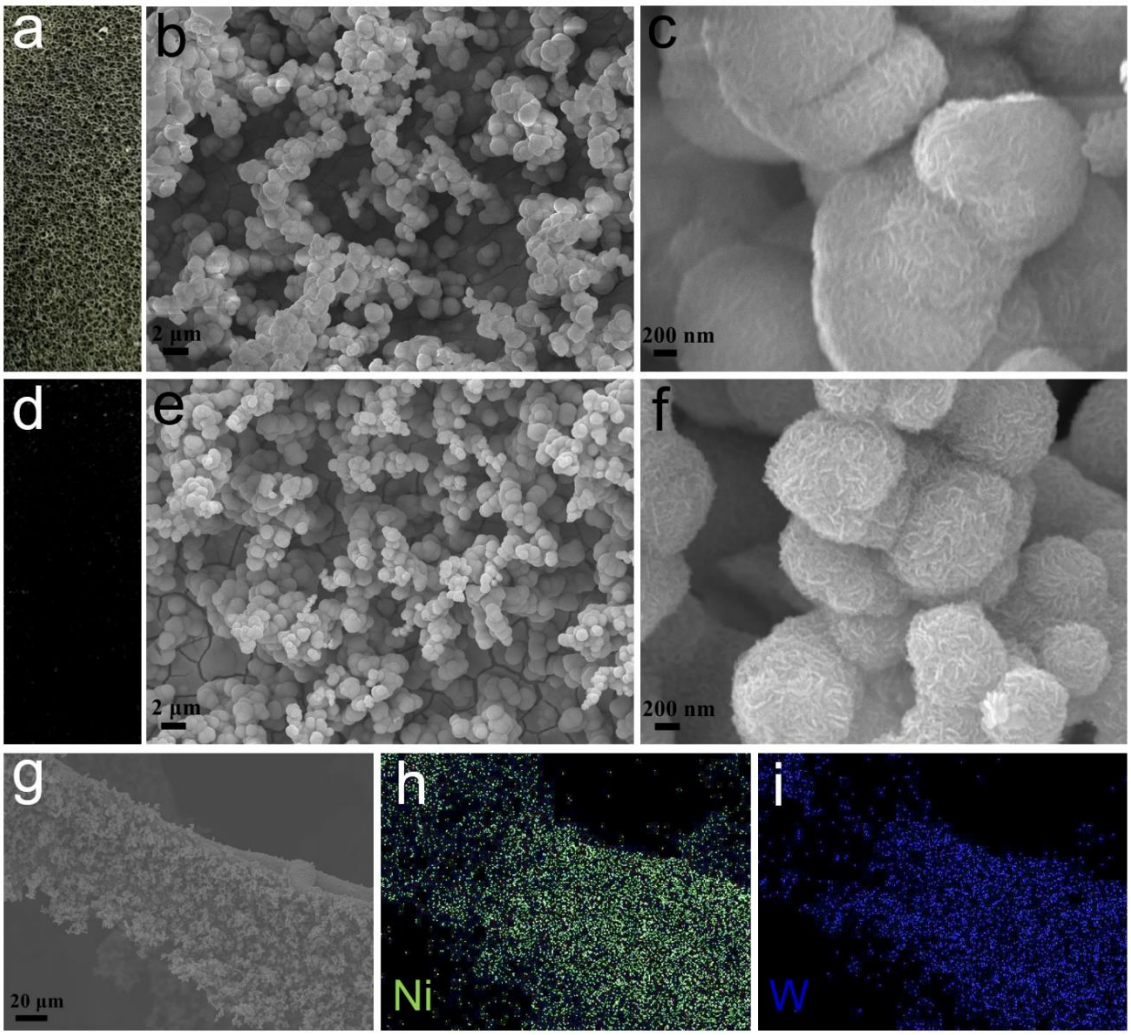

Supplementary Fig. S24. (a) Photograph and (b-c) SEM images of the NiW LDH precursor. (d) Photograph and (e-g) SEM images of the NiW-H_2 catalyst. (h) Ni and (i) W EDS mapping images corresponding to (g).

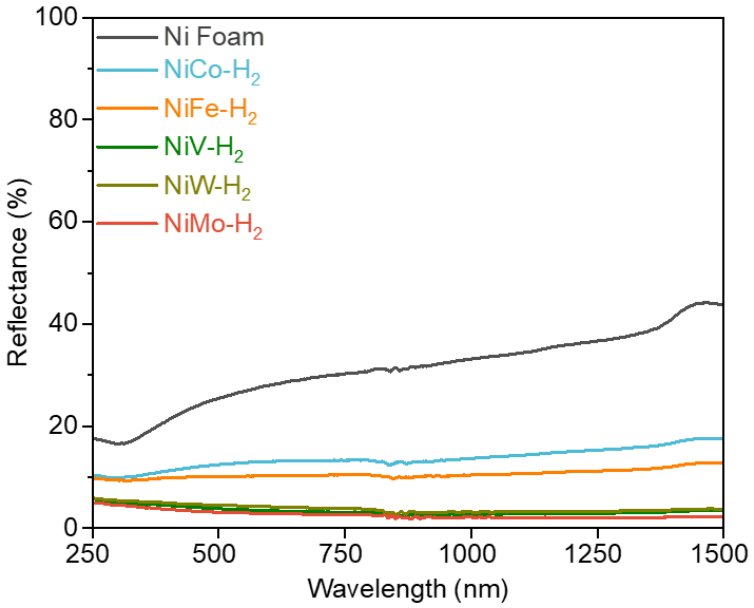

Supplementary Fig. S25. UV–vis–NIR reflectance spectra for the Ni foam substrate and NiX-H_2 (X = Co, Fe, V, W, and Mo) catalysts.

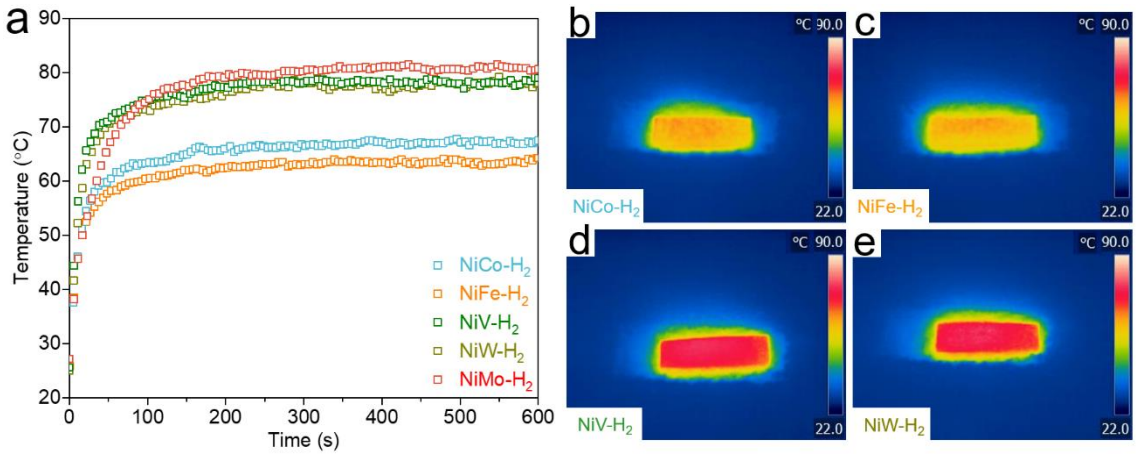

Supplementary Fig. S26. (a) Temperature evolution curves for NiX-H_2 (X = Co, Fe, V, W, and Mo) catalysts under simulated one sun irradiation. Infrared images of (b) NiCo-H_2, (c) NiFe-H_2, (d) NiV-H_2, and (e) NiW-H_2 catalysts during exposure to simulated one sun irradiation for 600 s.

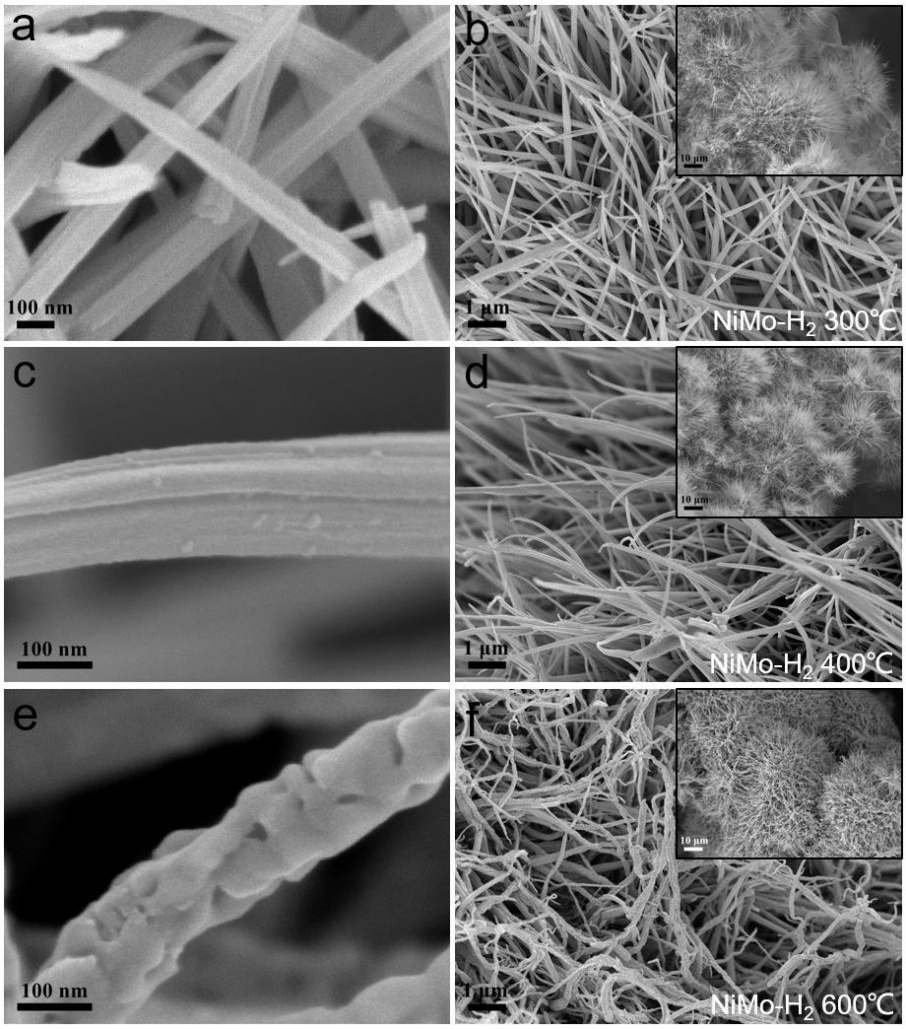

Supplementary Fig. S27. SEM images of NiMo-H_2 catalysts subjected to hydrogen reduction at (a-b) 300, (c-d) 400, and (e-f) 600 °C.

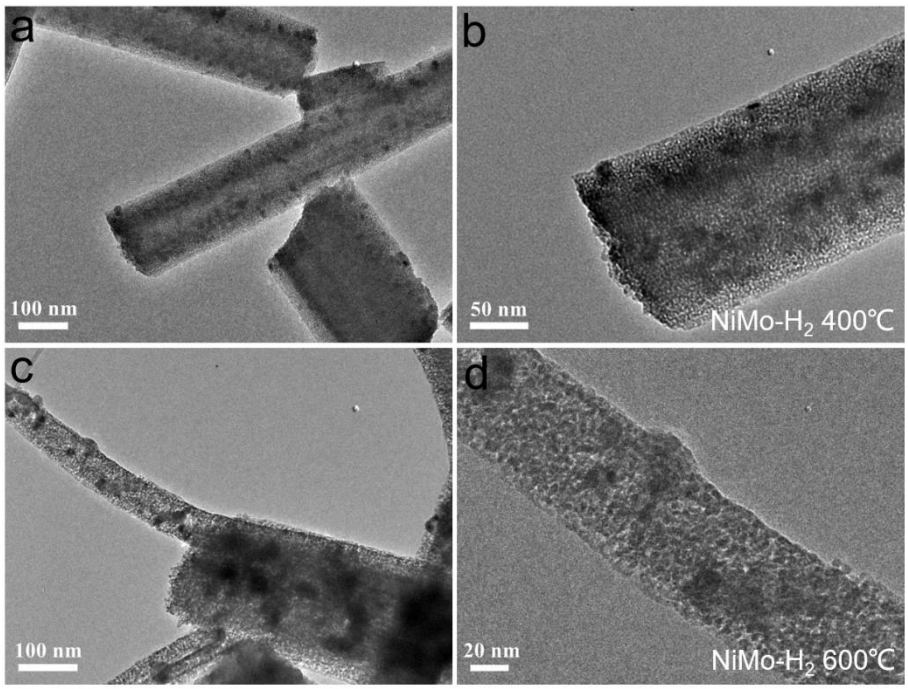

Supplementary Fig. S28. TEM images of NiMo-H_2 catalysts subjected to hydrogen reduction at (a-b) 400 and (c-d) 600 °C.

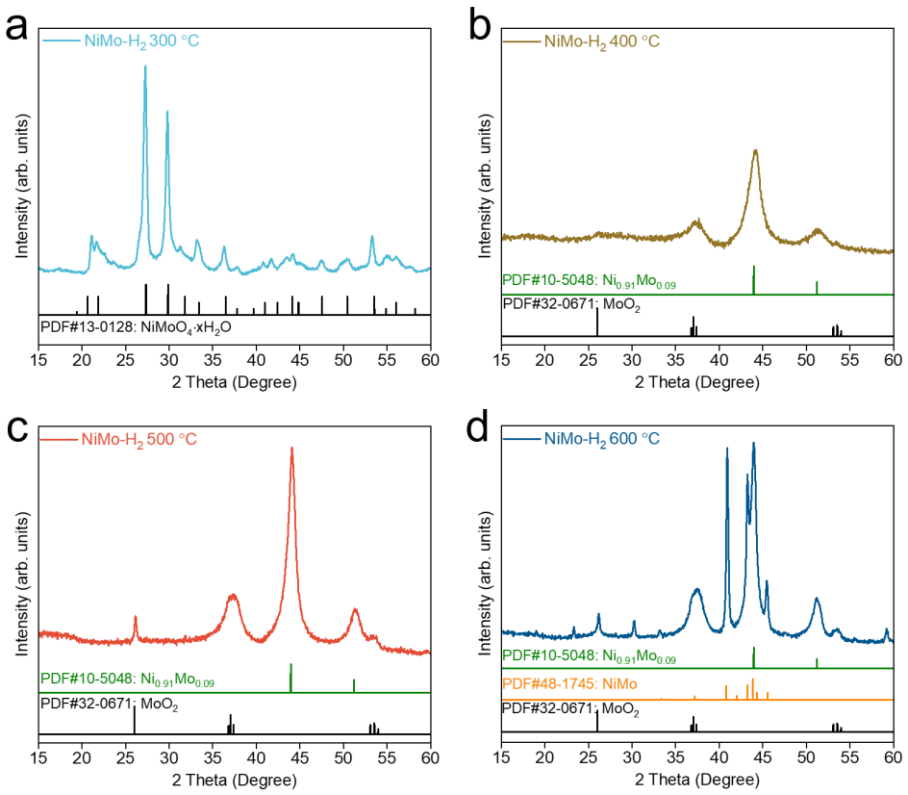

Supplementary Fig. S29. XRD patterns of powdered NiMo-H_2 catalysts subjected to hydrogen reduction at (a) 300, (b) 400, (c) 500, and (d) 600 °C.

XRD analysis shows that hydrogen reduction at 300 °C is insufficient for forming Ni-Mo alloy phase. At 400 and 500 °C, $Ni_{0.91}Mo_{0.09}$ and MoO_2 phases are successfully formed, with the sample reduced at 500 °C exhibiting enhanced crystallinity and achieving the best catalytic performance. Further increasing the reduction temperature to 600 °C leads to the formation of an additional NiMo phase.

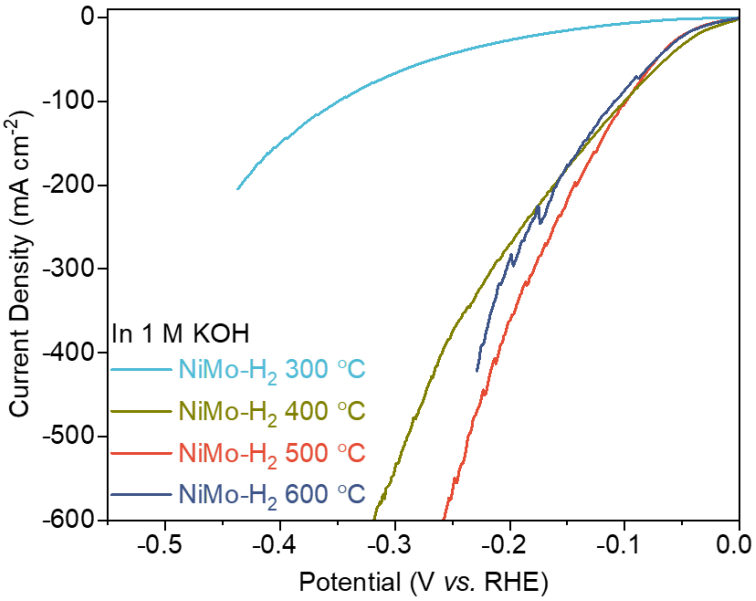

Supplementary Fig. S30. HER polarization curves for NiMo-H_2 catalysts subjected to hydrogen reduction at different temperatures.

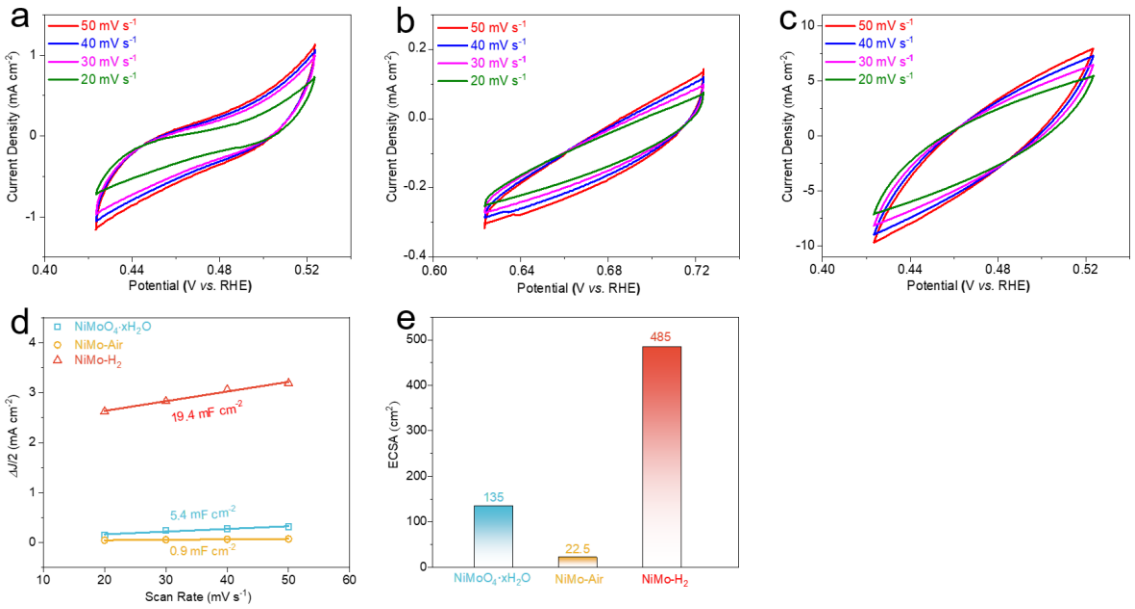

Supplementary Fig. S31. CV curves for (a) $NiMoO_4 \cdot xH_2O$, (b) NiMo-Air, and (c) NiMo-H_2 samples at different scan rates in a non-Faradaic region. (d) Corresponding C_{dl} values for these catalysts calculated from (a-c). (e) ECSA values for these samples.

Calculation of ECSA for each sample:

$$ECSA = C_{dl}/C_s \quad (6)$$

$$ECSA_{NiMoO_4 \cdot xH_2O} = 5.4\ mF\ cm^{-2}/40\ \mu F\ cm^{-2} = 135\ cm^2_{ECSA}$$

$$ECSA_{NiMo\text{-}Air} = 0.9\ mF\ cm^{-2}/40\ \mu F\ cm^{-2} = 22.5\ cm^2_{ECSA}$$

$$ECSA_{NiMo\text{-}H_2} = 19.4\ mF\ cm^{-2}/40\ \mu F\ cm^{-2} = 485\ cm^2_{ECSA}$$

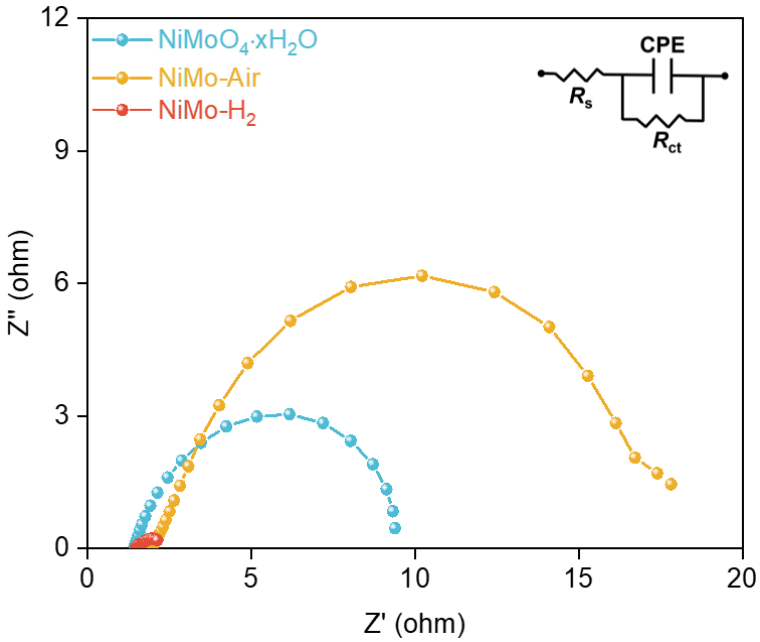

Supplementary Fig. S32. Nyquist plots for $NiMoO_4 \cdot xH_2O$, NiMo-Air, and NiMo-H_2 samples in 1 M KOH electrolyte. Inset: equivalent circuit.

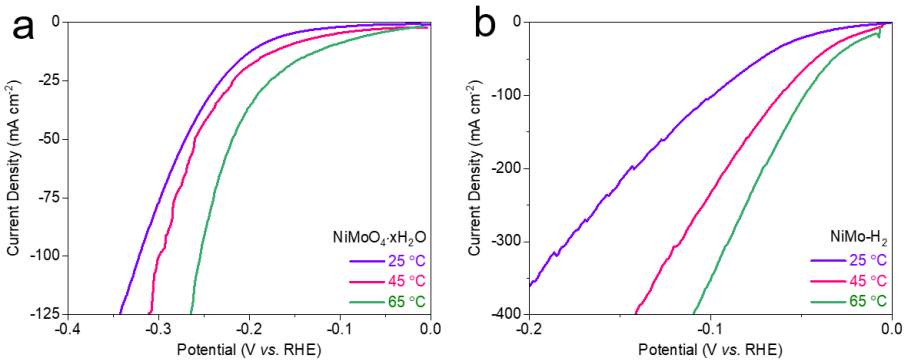

Supplementary Fig. S33. HER polarization curves for (a) $NiMoO_4 \cdot xH_2O$ and (b) NiMo-H_2 samples in 1 M KOH electrolyte at different temperatures.

The electrochemical active energy (E_a, kJ mol^{-1}) for HER catalysis is calculated using the Arrhenius equation as follows:

$$\frac{\partial\{\log(j)\}}{\partial\left(\frac{1}{T}\right)} = -\frac{E_a}{2.303\,R} \tag{7}$$

$$\text{or } E_a = -2.303 \times R \times \frac{\partial\{\log(j)\}}{\partial\left(\frac{1}{T}\right)} \tag{8}$$

where j is the current density (mA cm^{-2}) at a given potential, T is the temperature (K), and R is the gas constant (8.3145 J mol^{-1} K^{-1}).

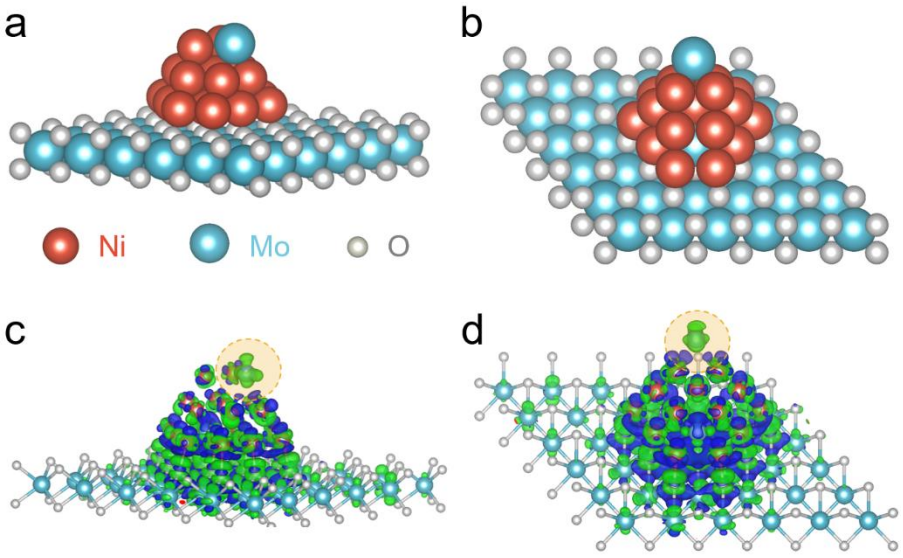

Supplementary Fig. S34. (a) Side and (b) top views of the NiMo-H_2 model for DFT calculations. (c) Side and (d) top views of charge density differences in NiMo-H_2. Green and blue regions represent electron accumulation and depletion, respectively.

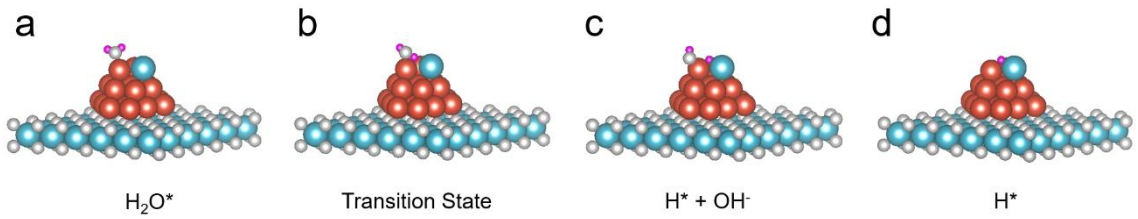

Supplementary Fig. S35. Structure models for (a) water adsorption, (b) transition state, (c) water dissociation, and (d) hydrogen adsorption over the Ni site in NiMo-H_2 for alkaline HER.

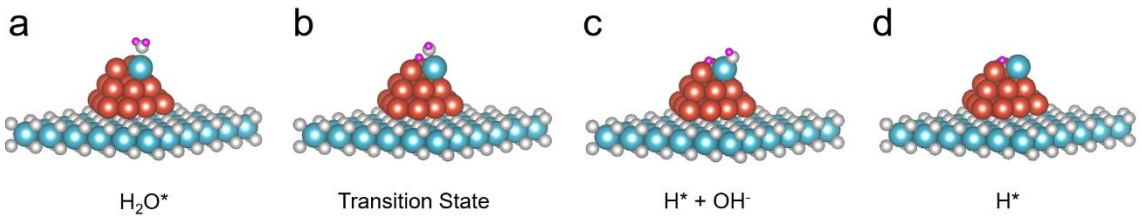

Supplementary Fig. S36. Structure models for (a) water adsorption, (b) transition state, (c) water dissociation, and (d) hydrogen adsorption over the Mo site in NiMo-H_2 for alkaline HER.

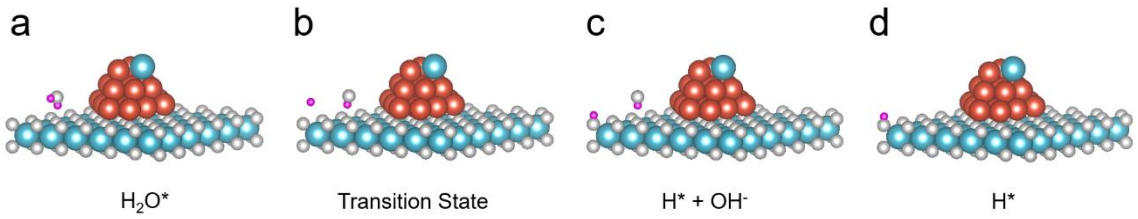

Supplementary Fig. S37. Structure models for (a) water adsorption, (b) transition state, (c) water dissociation, and (d) hydrogen adsorption over the O site in NiMo-H_2 for alkaline HER.

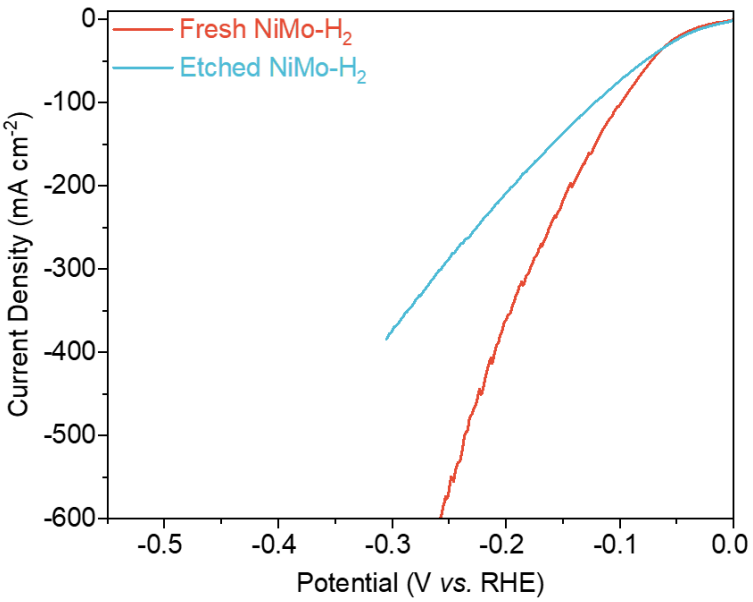

Supplementary Fig. S38. HER polarization curves for fresh and etched NiMo-H_2 samples in 1 M KOH electrolyte.

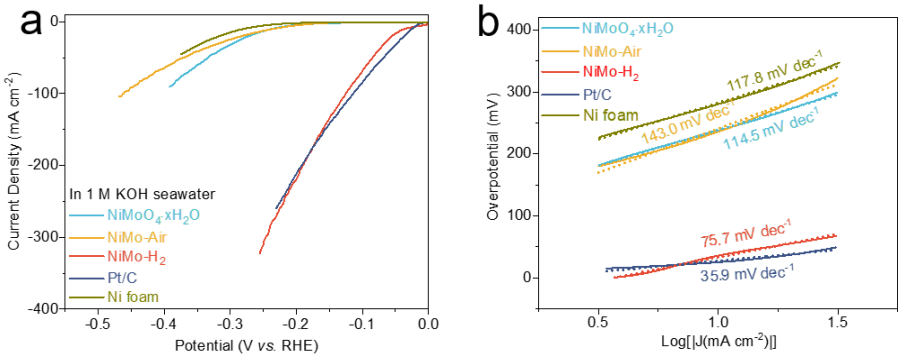

Supplementary Fig. S39. (a) HER polarization curves and (b) corresponding Tafel plots for $NiMoO_4 \cdot xH_2O$, NiMo-Air, NiMo-H_2, and Pt/C catalysts as well as Ni foam in 1 M KOH seawater electrolyte. J is the current density.

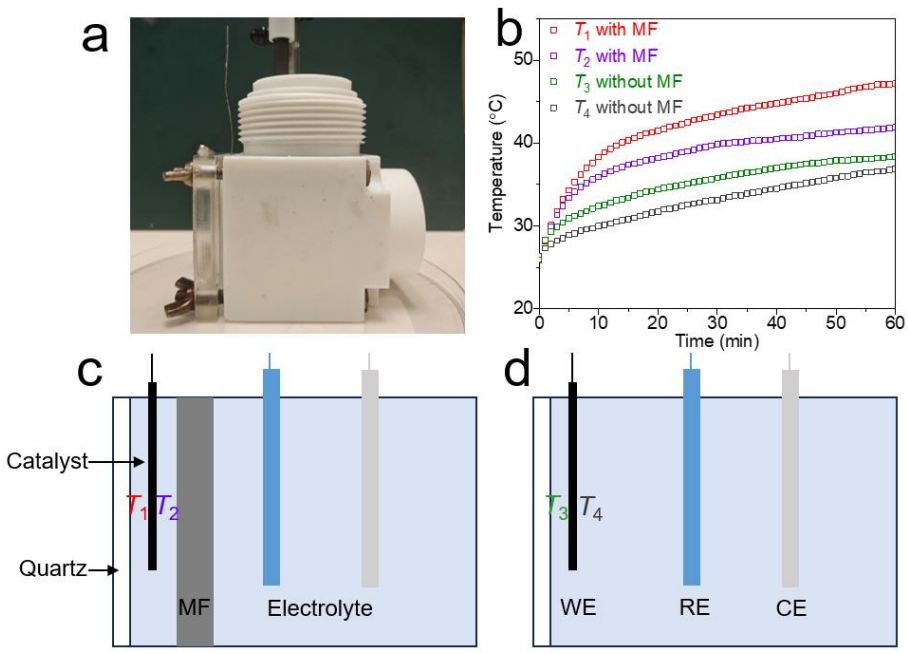

Supplementary Fig. S40. (a) Photograph of the homemade three-electrode photothermal electrolyzer. (b) Temperature evolution curves for different regions inside the photothermal electrolyzer as marked in (c) and (d) under one sun irradiation. Schematic illustrations of the side view of the photothermal electrolyzer (c) with and (d) without melamine foam (MF) used as a thermal insulation layer. WE, RE, and CE in (d) represent the working, reference, and counter electrodes, respectively.

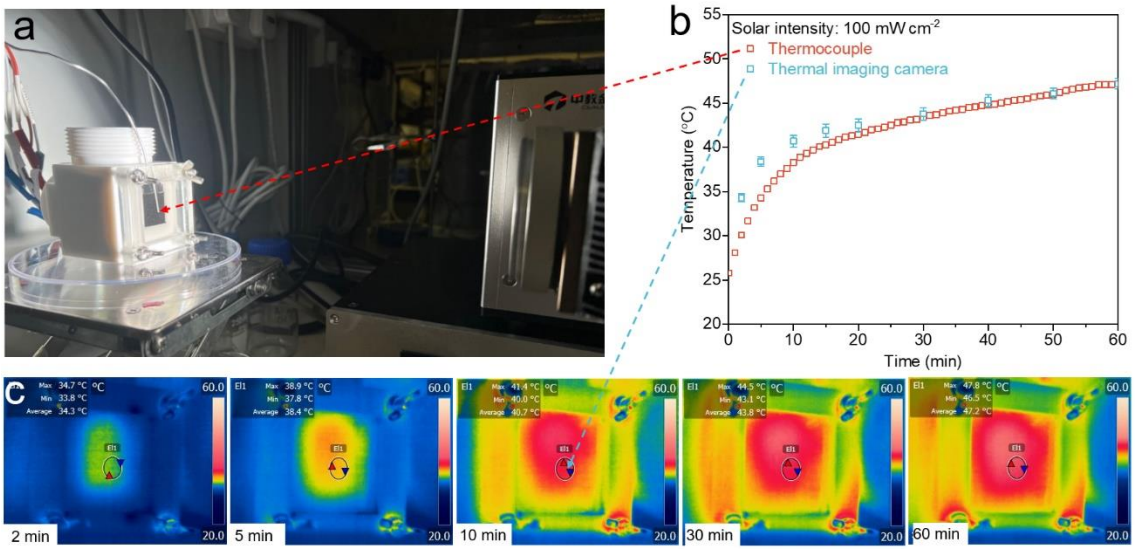

Supplementary Fig. S41. (a) Photograph of the procedure for photothermal electrolyzer temperature measurement. (b) Temperature evolution curves for the bulk electrolyte and the NiMo-H_2 catalyst under simulated one sun irradiation measured using a thermocouple and a thermal imaging camera, respectively. (c) Infrared images of the NiMo-H_2 catalyst under light irradiation for different amounts of time.

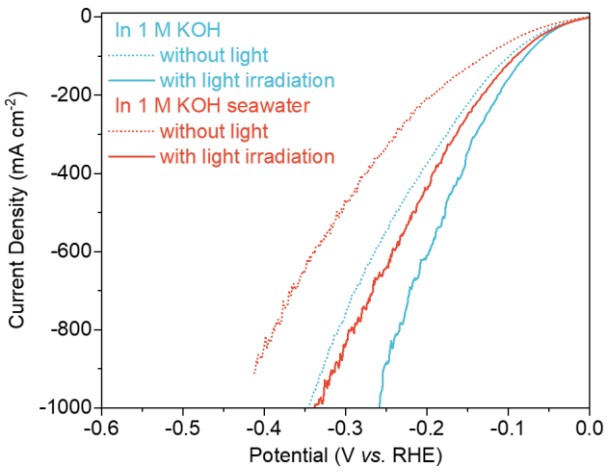

Supplementary Fig. S42. Large-current HER polarization curves of NiMo-H_2 catalyst in 1 M KOH and 1 M KOH seawater electrolytes with and without light irradiation.

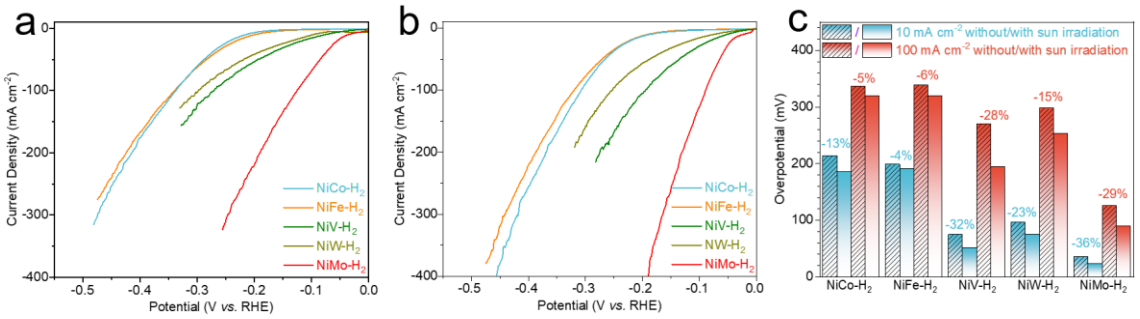

Supplementary Fig. S43. HER polarization curves for NiX-H_2 catalysts in 1 M KOH seawater (a) without light irradiation and (b) under simulated one sun irradiation. (c) Overpotentials required by NiX-H_2 catalysts to attain current densities of 10 and 100 mA cm^{-2} in 1 M KOH seawater without and with light irradiation.

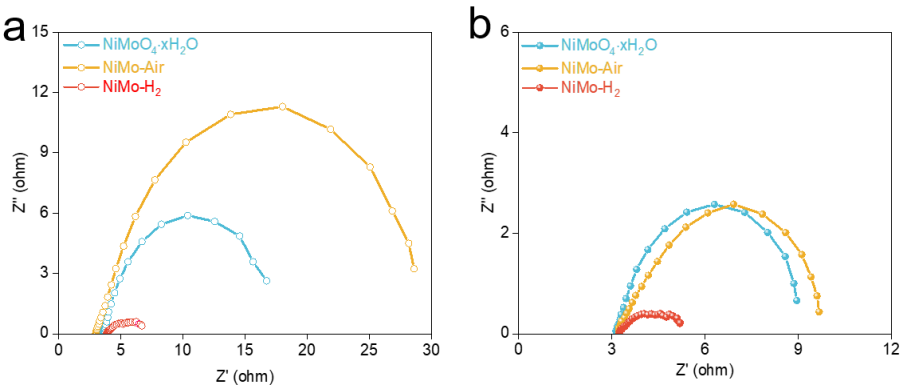

Supplementary Fig. S44. Nyquist plots for $NiMoO_4 \cdot xH_2O$, NiMo-Air, and $NiMo\text{-}H_2$ catalysts in 1 M KOH seawater (a) without light irradiation and (b) under simulated one sun irradiation.

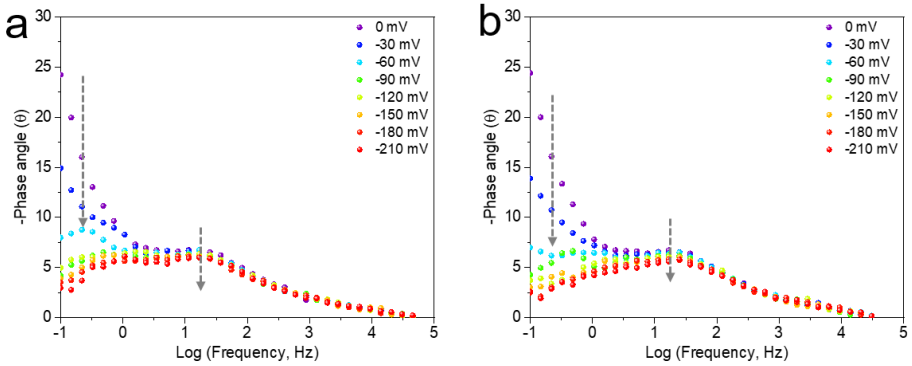

Supplementary Fig. S45. Potential-dependent EIS Bode plots for the NiMo-H_2 catalyst in 1 M KOH seawater (a) without and (b) with light irradiation.

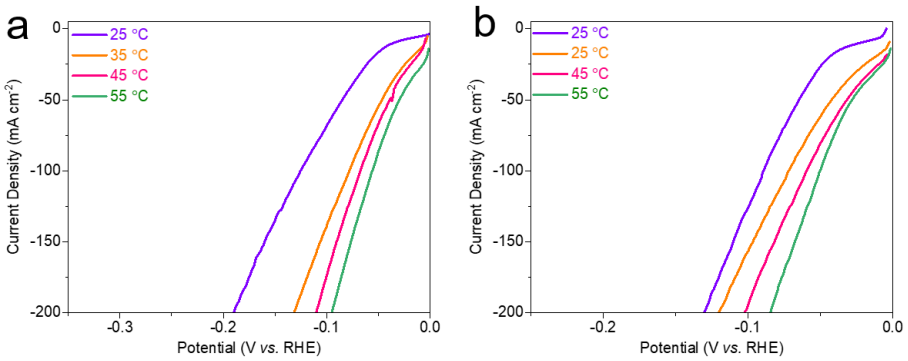

Supplementary Fig. S46. HER polarization curves for the NiMo-H_2 catalyst in 1 M KOH seawater (a) without light irradiation and (b) under simulated one sun irradiation at different temperatures.

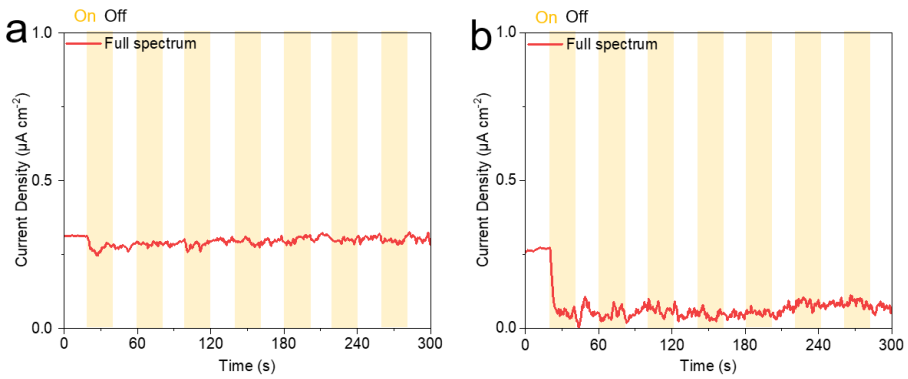

Supplementary Fig. S47. Photocurrent measurement of (a) the $NiMoO_4 \cdot xH_2O$ precursor and (b) the NiMo-H_2 catalyst in 1 M KOH electrolyte under chopped full spectrum light irradiation. Yellow regions represent durations of time under irradiation.

To measure the photocurrent of the $NiMoO_4 \cdot xH_2O$ precursor and the NiMo-H_2 catalyst, fluorine-doped tin oxide (FTO) electrodes based on each were prepared by a drop-casting method. In detail, each sample was dissolved in a mixed solution containing 990 μL ethanol and 10 μL Nafion 117 solution, which was then dripped onto the surface of a FTO glass plate and dried at 40 °C. The photocurrent was measured under chopped full spectrum illumination using a two-electrode configuration, with a FTO electrode serving as the photoanode and a Pt plate serving as the counter electrode, in 1 M KOH electrolyte.

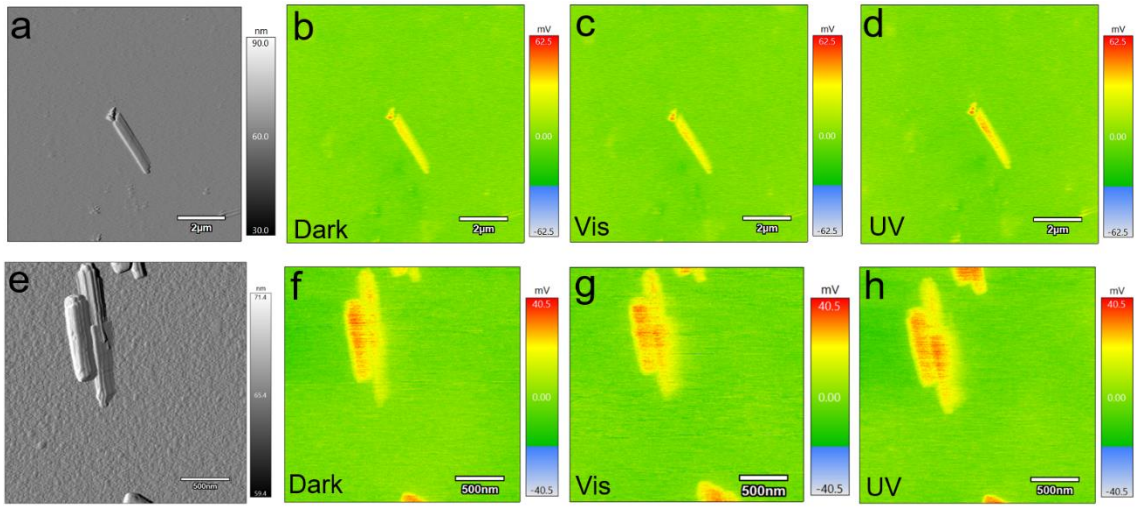

Supplementary Fig. S48. (a) Topography of the $NiMoO_4 \cdot xH_2O$ precursor and its contact potential (b) in the dark, (c) under visible light, and (d) under UV light irradiation. (e) Topography of the NiMo-H_2 catalyst and its contact potential (f) in the dark, (g) under visible light, and (h) under UV light irradiation.

When full-spectrum solar irradiation is applied to a catalyst, in addition to the photothermal effect, the photoelectric effect may also contribute to promoting catalytic reactions. Therefore, we first conducted photocurrent testing to detect whether the NiMo-H_2 catalyst exhibits the photoelectric effect. As shown Fig. S47, no photocurrent was observed for either the $NiMoO_4 \cdot xH_2O$ precursor or the NiMo-H_2 catalyst under chopped full spectrum light irradiation. AFM was then utilized to examine any change in its contact potential caused by light illumination. As presented in Fig. S48, neither the contact potential of the $NiMoO_4 \cdot xH_2O$ precursor nor that of the NiMo-H_2 catalyst showed any obvious change under dark, visible, or UV light irradiation conditions. Therefore, it can be concluded that the NiMo-H_2 catalyst does not exhibit the photoelectric effect under light irradiation and that the enhancement of its catalytic performance should result from the photothermal effect.

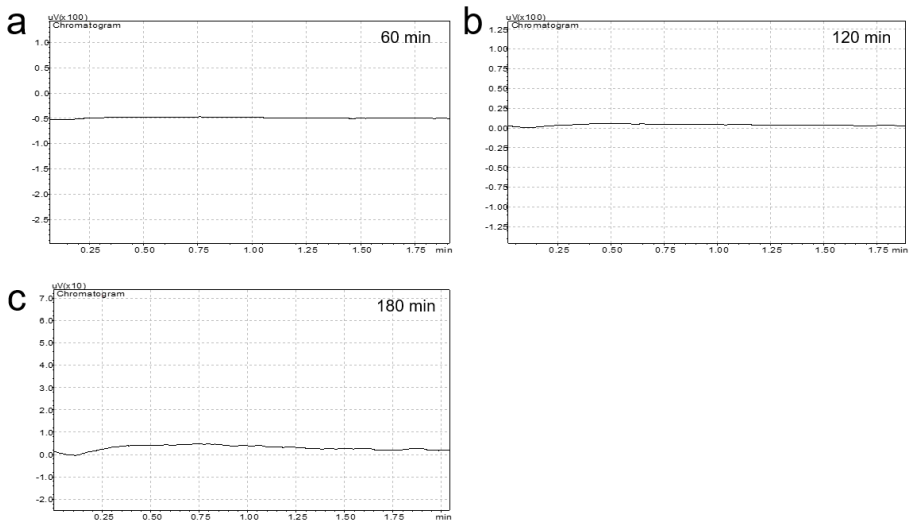

Supplementary Fig. S49. Gas chromatography curves of the NiMo-H_2 catalyst in 180 min photocatalytic H_2 production testing. If H_2 gas is detected, a peak should be seen at ~1.3 min.

The photocatalytic activity of the NiMo-H_2 catalyst was evaluated by dispersing 10 mg NiMo-H_2 powder in 10 ml of 1 M KOH solution in a sealed quartz vial. Before the measurement, the quartz vial was purged with Ar gas for 15 min to eliminate the air. The photocatalytic H_2 generation was then measured under full spectrum light from a 300 W Xe lamp (CEL-PE300E-3A) with an intensity of 100 mW cm^{-2} (simulated one sun irradiation). The reactor was syringed drawn (100 μl) every around 30 min to measure the H_2 gas amount using a gas chromatography (Shimadzu, GC-2014AT).

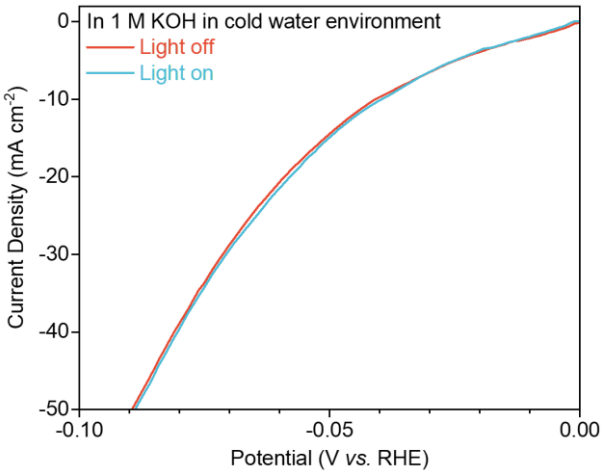

Supplementary Fig. S50. HER polarization curves of NiMo-H_2 catalyst in 1 M KOH in a cold water environment under different light irradiation conditions.

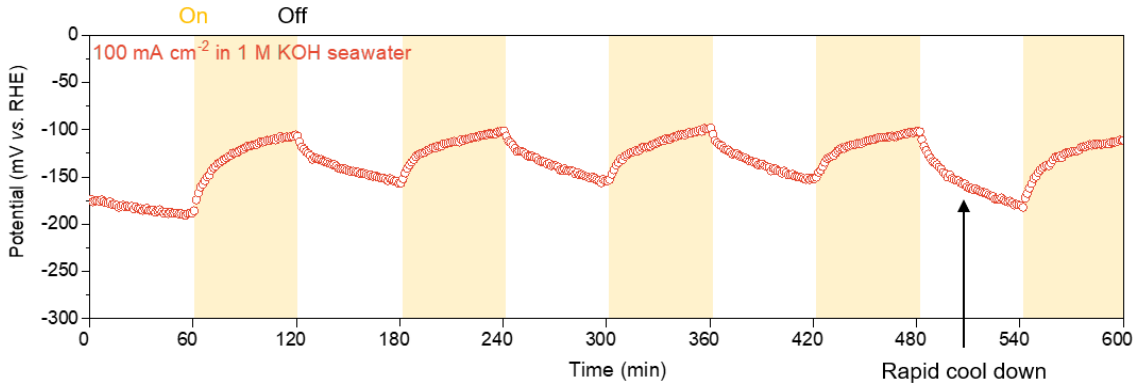

Supplementary Fig. S51. Chronopotentiometric curve for the NiMo-H_2 catalyst at a constant current density of 100 mA cm^{-2} in 1 M KOH seawater under chopped illumination for HER. Yellow regions represent durations of time under illumination.

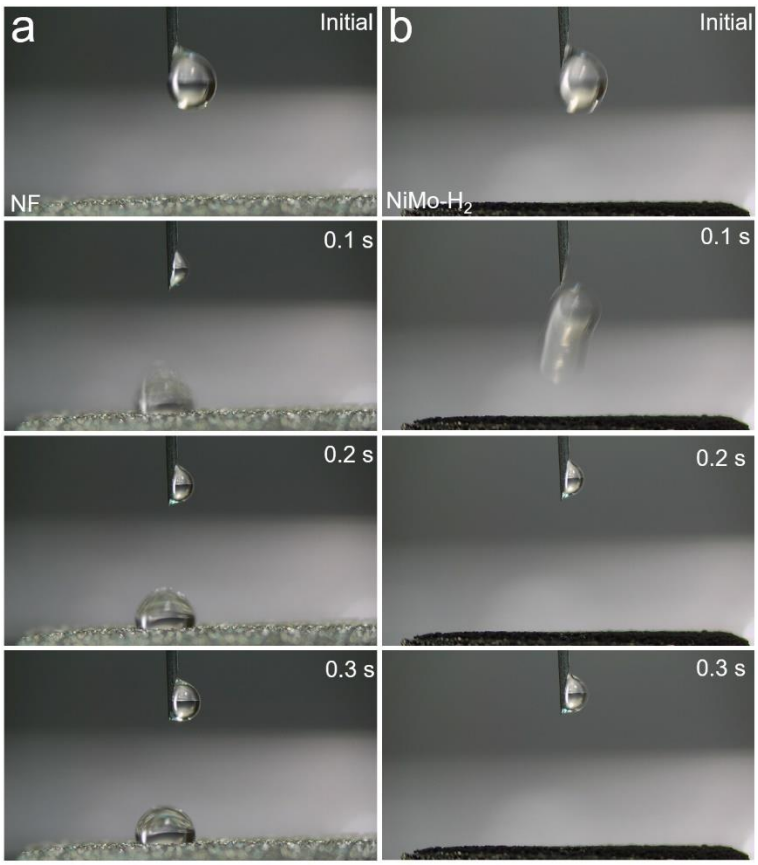

Supplementary Fig. S52. Digital images of a droplet of KOH solution placed on the surface of (a) the NF substrate and (b) the NiMo-H_2 catalyst.

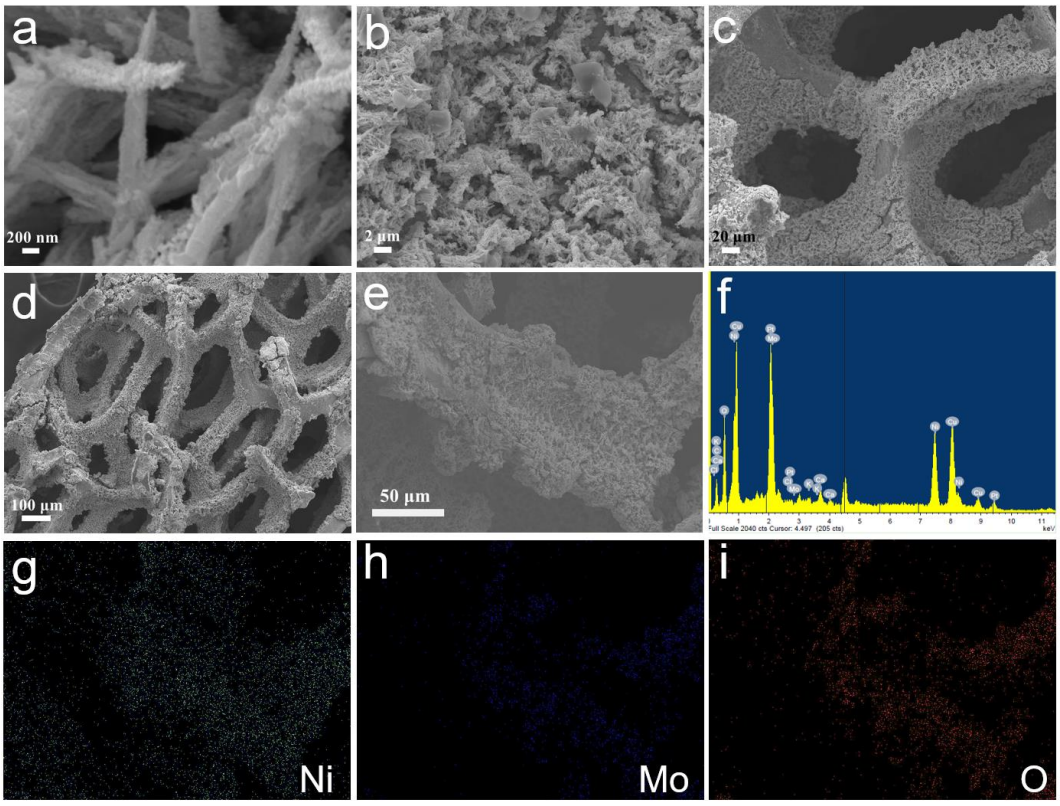

Supplementary Fig. S53. (a-e) SEM images of the NiMo-H_2 catalyst after 540 h of durability testing at a constant current density of 500 mA cm^{-2} in 6 M KOH seawater under simulated one sun irradiation. (f) EDS spectrum and (g) Ni, (h) Mo, and (i) O EDS mapping images corresponding to (e). The Pt signal comes from the Pt coating in the SEM sample preparation process and the Cu signal comes from the CF substrate.

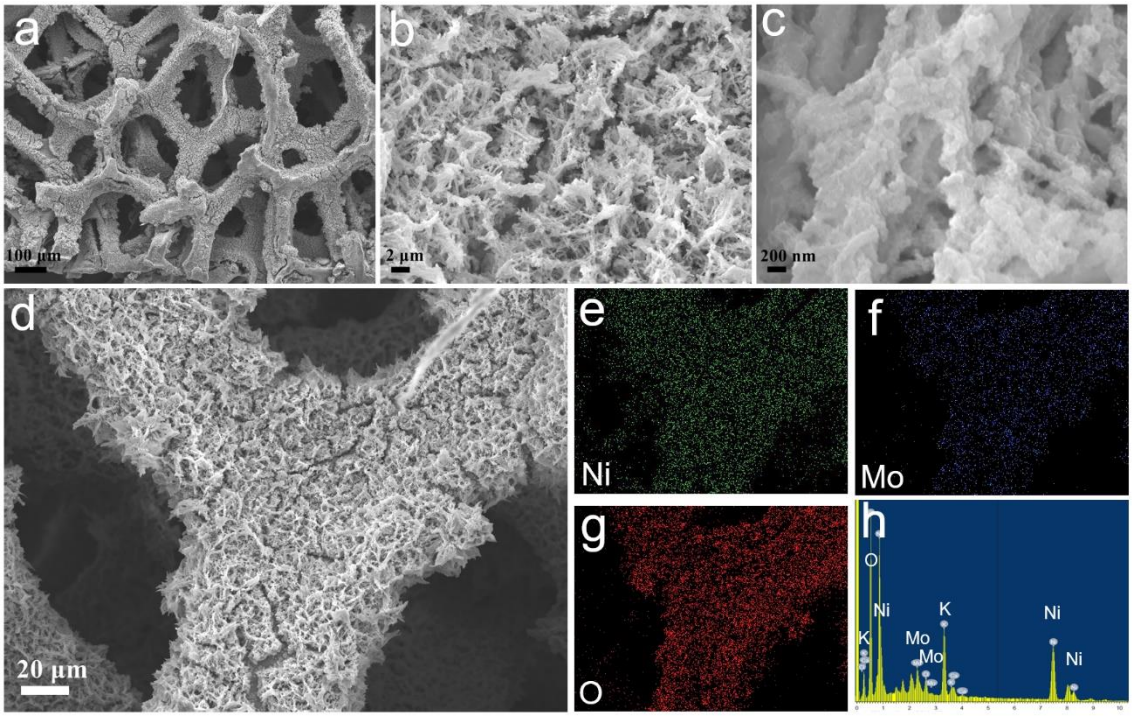

Supplementary Fig. S54. (a-d) SEM images of the NiMo-H_2 catalyst after 26 h of durability testing at a constant current density of 200 mA cm^{-2} in 1 M KOH seawater under simulated one sun irradiation. (e) Ni, (f) Mo, and (g) O EDS mapping images and (h) EDS spectrum corresponding to (d).

a

Sample	Ni : Mo (atomic ratio)
Fresh NiMo-H_2	1.14:1
Post NiMo-H_2	1.33:1

b

Sample	Ni (PPM)	Mo (PPM)
Fresh 1 M KOH seawater (diluted to 1%)	Not Detected	0.05
Post 1 M KOH seawater (diluted to 1%)	Not Detected	0.73

Supplementary Fig. S55. (a) Ni : Mo ratio in the fresh and post-reaction NiMo-H_2 catalyst measured using ICP spectroscopy. (b) Elemental Ni and Mo in the fresh and post-reaction 1 M KOH seawater electrolyte (diluted to 1% concentration) measured using ICP spectroscopy.

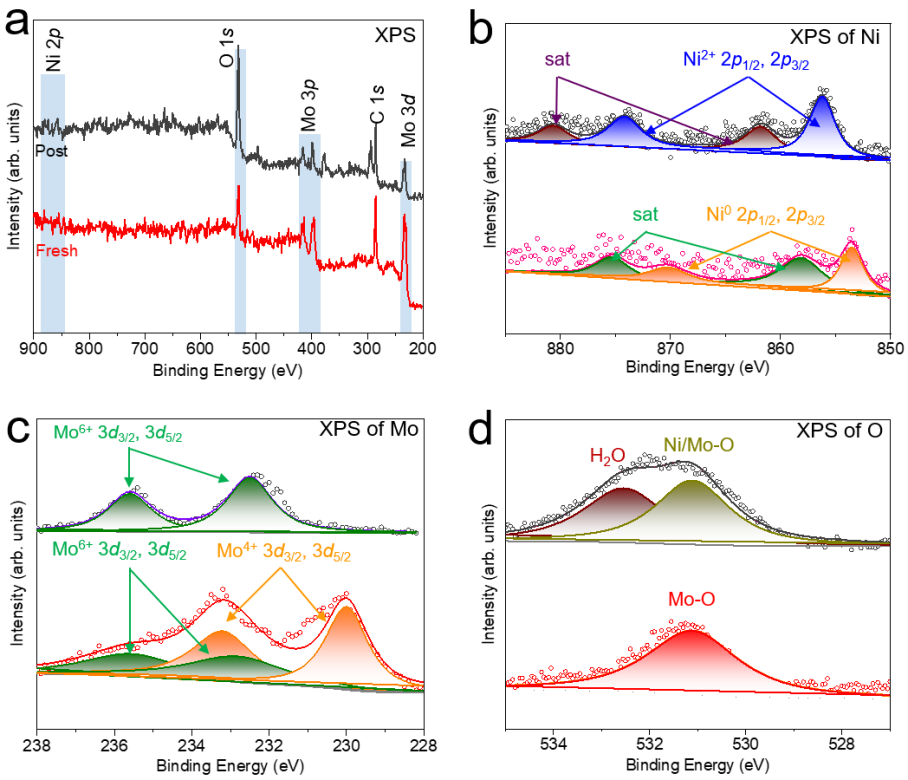

Supplementary Fig. S56. (a) Overall and high-resolution XPS spectra of (b) Ni, (c) Mo, and (d) O for the NiMO-H_2 catalyst before (bottom) and after (top) 26 h of durability testing at a constant current density of 200 mA cm^{-2} in 1 M KOH seawater under simulated one sun irradiation.

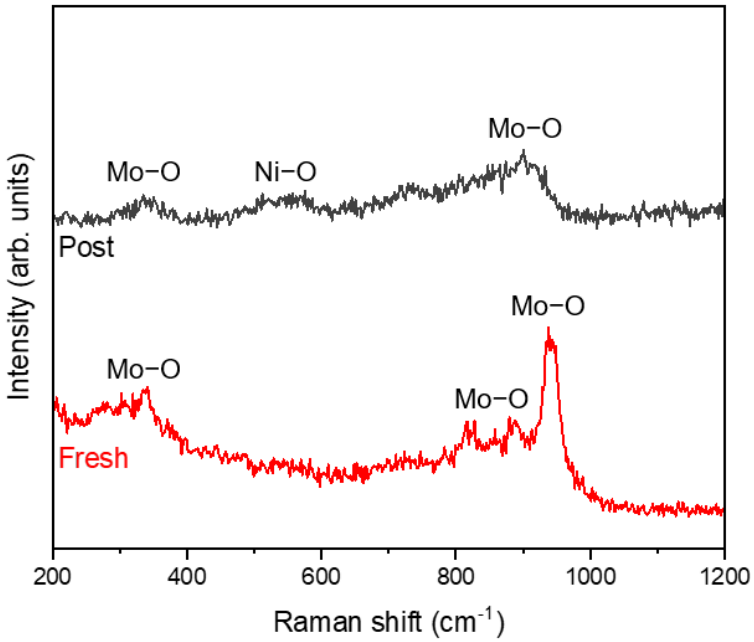

Supplementary Fig. S57. Raman spectra for the NiMo-H_2 catalyst before and after 26 h of durability testing at a constant current density of 200 mA cm^{-2} in 1 M KOH seawater under simulated one sun irradiation.

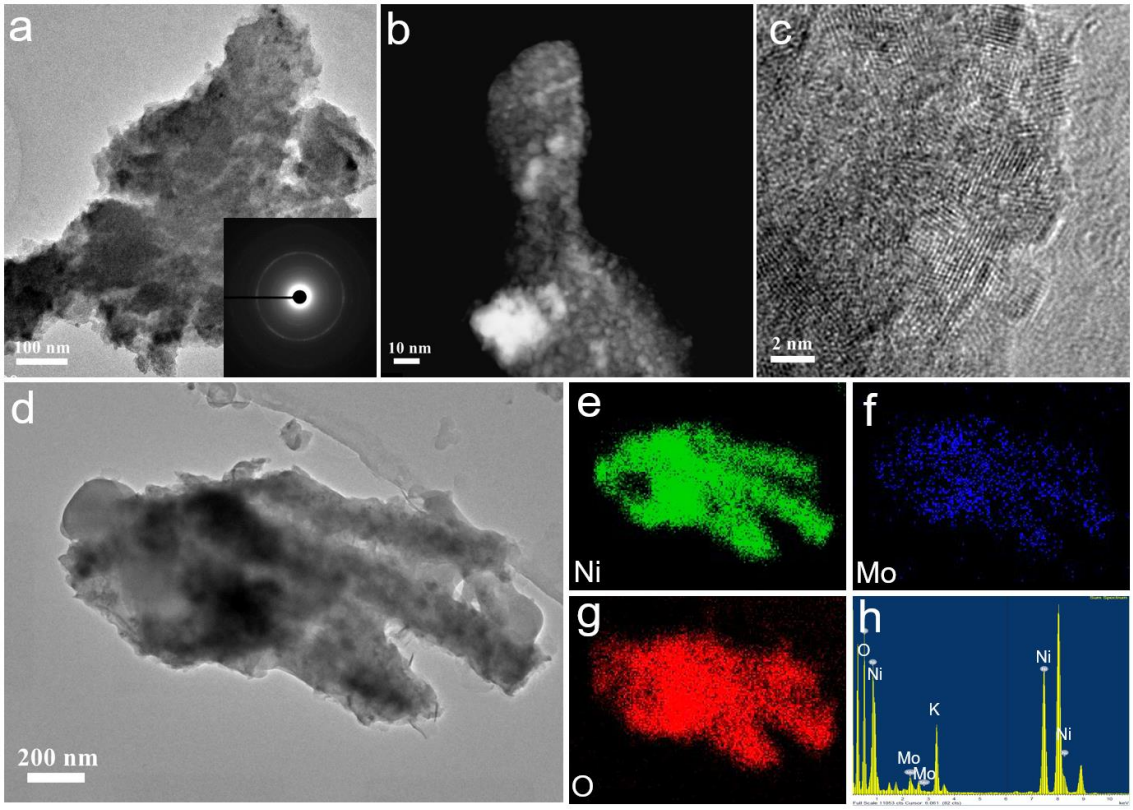

Supplementary Fig. S58. (a-d) TEM images and [(inset to (a)] SAED pattern for the NiMo-H_2 catalyst after 26 h of durability testing at a constant current density of 200 mA cm^{-2} in 1 M KOH seawater under simulated one sun irradiation. (e) Ni, (f) Mo, and (g) O EDS mapping images and (h) EDS spectrum corresponding to (d).

Various characterization methods were used to analyze the morphology and composition changes in the NiMo-H_2 catalyst after photothermal-promoted catalytic reactions. SEM images in Fig. S54a–d indicate that the original nanorod structure was maintained, despite the appearance of some cracks, after 26 h of catalytic durability testing in 1 M KOH seawater under simulated one sun irradiation. The corresponding EDS mapping images and spectrum in Fig. S54e–h reveal that elemental Ni, Mo, and O could be detected after the durability test. The detailed ICP analyses in Fig. S55 shows that the Ni : Mo ratio became higher and more elemental Mo could be detected in the electrolyte after the catalytic reaction, both of which indicate the reduction of elemental Mo in the catalyst post-reaction. A comparison of XPS spectra before and after durability testing

indicates that both Ni and Mo were oxidized to higher valence states following testing (Fig. S56), accompanied by an increase in the intensity of elemental O. Specifically, after the durability test, the valence of elemental Ni was oxidized from 0 to 2+ (Fig. S56b), the valence of elemental Mo was oxidized from 4+ to 6+ (Fig. S56c), and the XPS peak for elemental O became broader (Fig. S56d). The composition of the catalyst after durability testing was then analyzed using Raman spectroscopy, which revealed a decrease in the intensity of the M–O peaks, along with the appearance of Ni–O peaks for $Ni(OH)_2$ (Fig. S57). The ring SAED pattern and HRTEM images in the TEM analysis shown in Fig. S58 further reveal that the NiMo-H_2 catalyst became partially amorphous following durability testing and that nanoparticles were formed on the nanorods. The above analyses indicate that when the NiMo-H_2 catalyst is employed for photothermal-promoted HER in alkaline seawater, some of the elemental Mo on its surface will leak into the electrolyte, and the constituent $Ni_{0.91}Mo_{0.09}$ alloy nanoparticles will transform into $Ni(OH)_2$ particles.

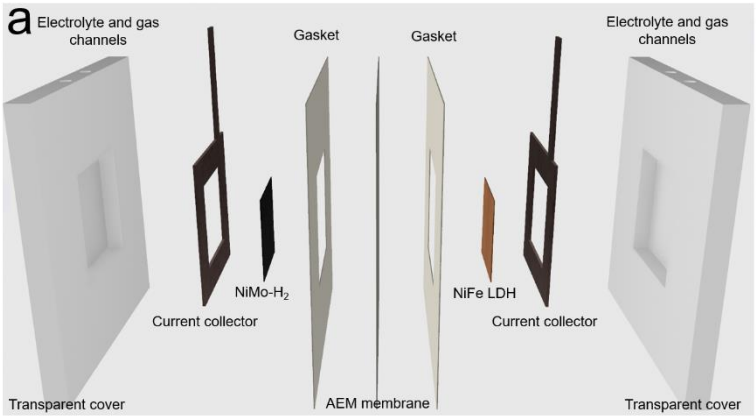

Supplementary Fig. S59. Schematic diagram of the homemade photothermal AEM electrolyzer.

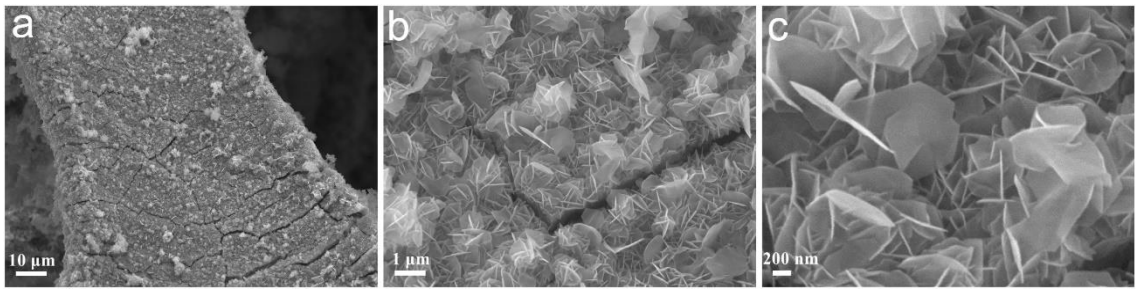

Supplementary Fig. S60. SEM images of the NiFe LDH catalyst for OER catalysis.

A NiFe LDH catalyst was synthesized as the OER catalyst to couple with NiMo-H_2 for photothermal-promoted overall alkaline seawater electrolysis. Briefly, 2 mmol $Ni(NO_3)_2 \cdot 6H_2O$, 2 mmol iron nitrate nonahydrate [$Fe(NO_3)_3 \cdot 9H_2O$, Sigma Aldrich], and 15 mmol $CO(NH_2)_2$ were dissolved homogeneously in 100 mL DI water in a beaker. A piece of NF was placed inside the beaker and then underwent a water bath reaction at 90 °C for 12 h. After cooling down, the resulting NiFe LDH was removed, rinsed with DI water, and dried in air.

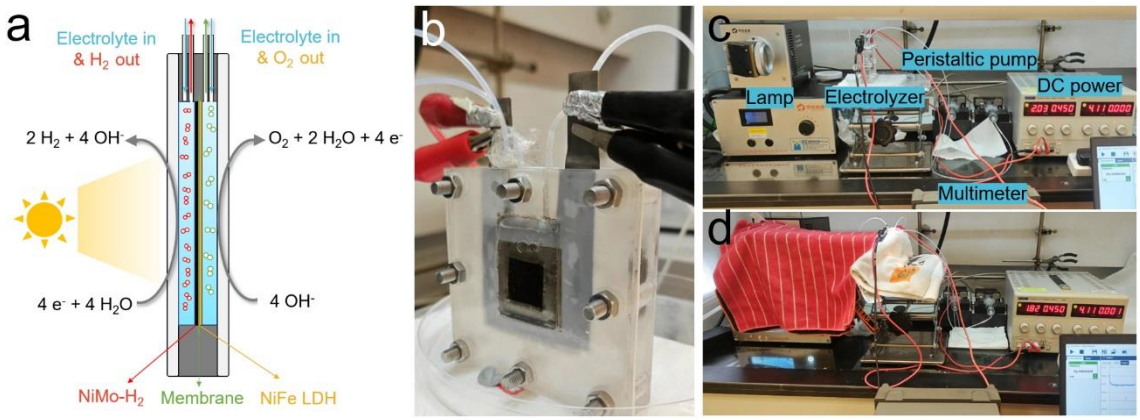

Supplementary Fig. S61. (a) Schematic illustration of the working mechanism for, and (b) photograph of, the photothermal AEM electrolyzer. Photographs of overall seawater electrolysis tests (c) without and (d) with light irradiation.

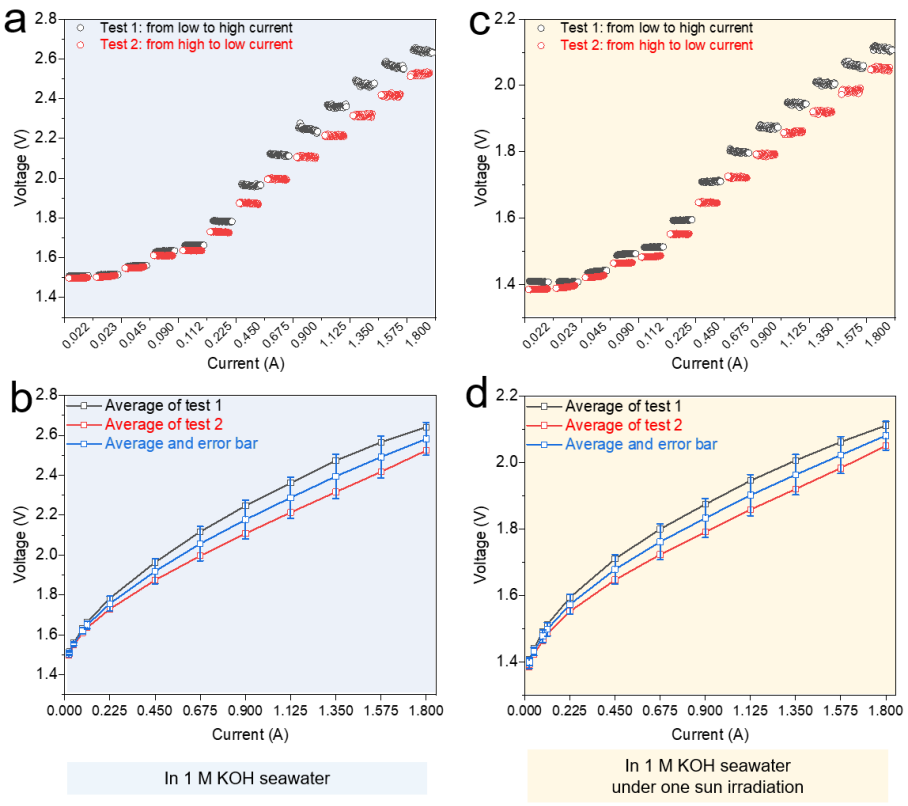

Supplementary Fig. S62. Overall seawater electrolysis performance by the NiMo-H_2||NiFe LDH pair (a-b) in 1 M KOH seawater and (c-d) in 1 M KOH seawater under simulated one sun irradiation. Error bars represent standard deviations from the mean of the tests in (a-b).

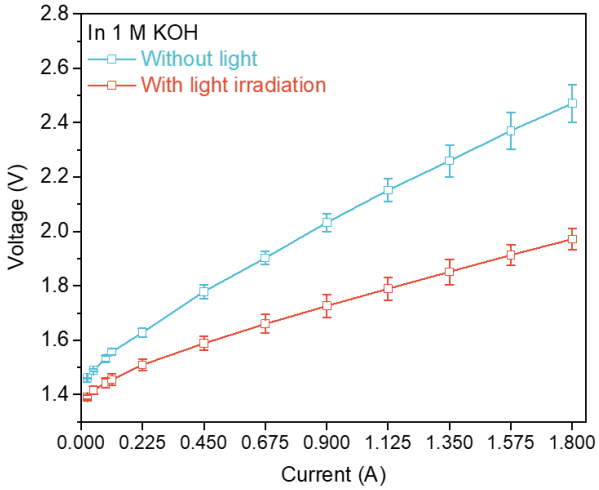

Supplementary Fig. S63. Overall freshwater electrolysis performance of the NiMo-H_2||NiFe LDH pair in 1 M KOH with and without light irradiation. Error bars represent standard deviations from the mean of the tests.

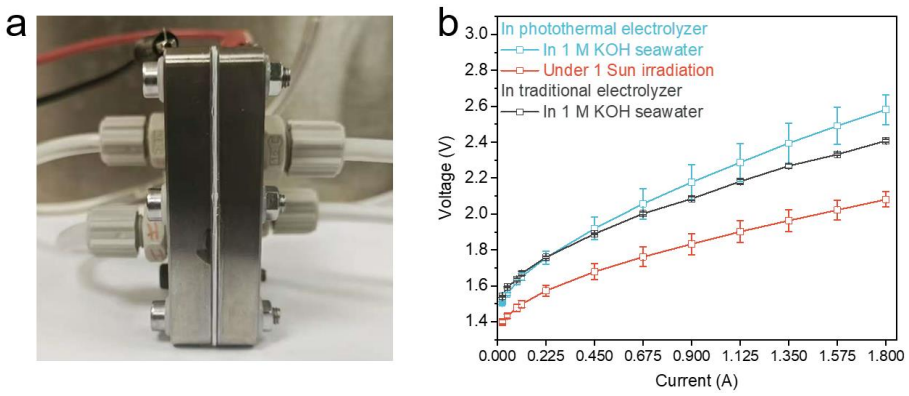

Supplementary Fig. S64. (a) Photograph of traditional AEM electrolyzer. (b) Overall seawater electrolysis performance of the NiMo-H_2||NiFe LDH pair in 1 M KOH seawater in different electrolyzers. Error bars represent standard deviations from the mean of the tests.

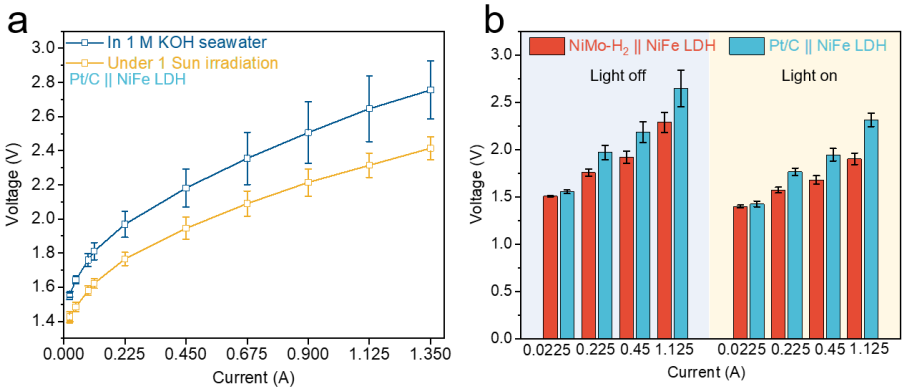

Supplementary Fig. S65. Overall seawater electrolysis performance of the (a) Pt/C||NiFe LDH pair in 1 M KOH seawater with and without light irradiation. Error bars represent standard deviations from the mean of the tests. (b) Comparison of the overall seawater electrolysis performance between NiMo-H_2||NiFe LDH and Pt/C||NiFe LDH pair.

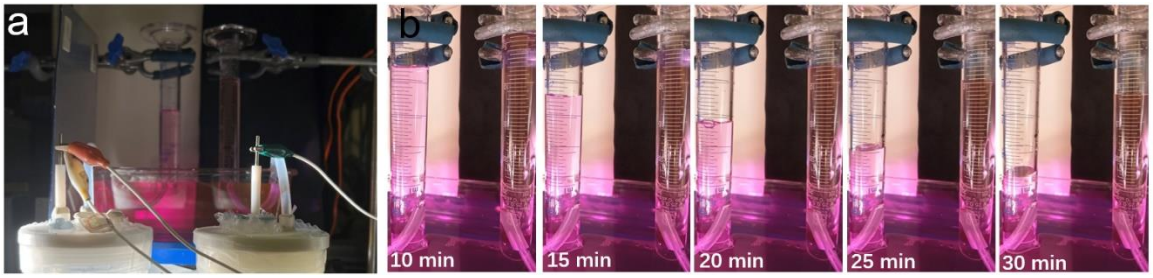

Supplementary Fig. S66. (a) Photograph of the FE testing apparatus for photothermal-promoted overall seawater electrolysis. (b) Photographs showing the amounts of gases collected at different durations of time.

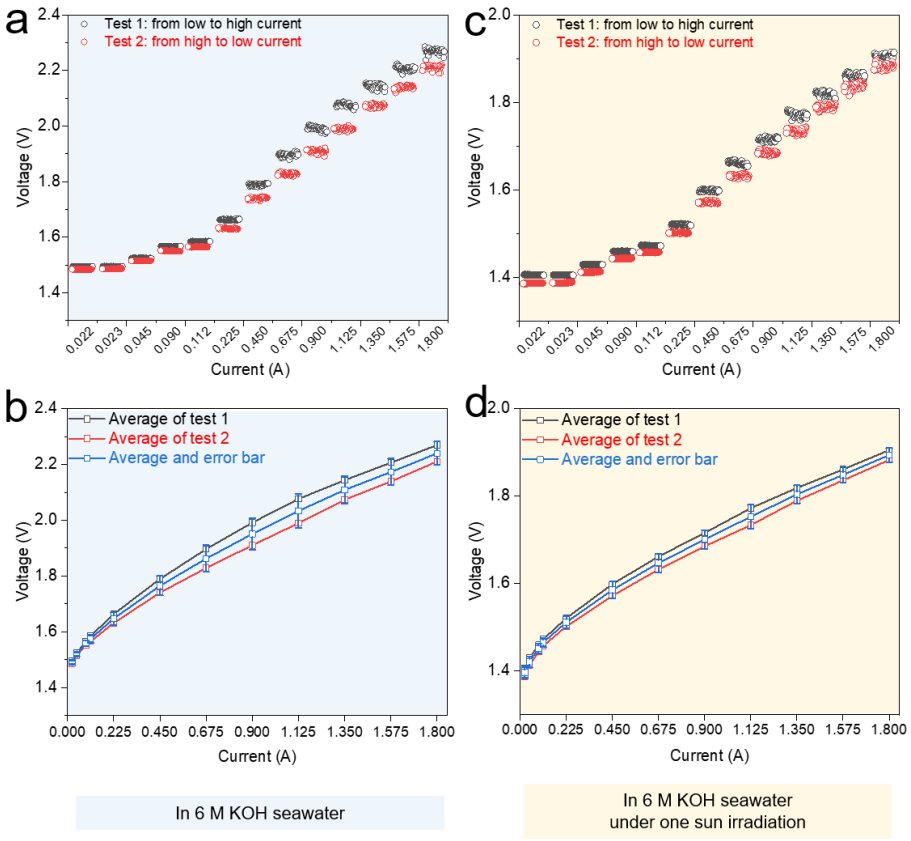

Supplementary Fig. S67. Overall seawater electrolysis performance by the NiMo-H_2||NiFe LDH pair (a-b) in 6 M KOH seawater and (c-d) in 6 M KOH seawater under simulated one sun irradiation. Error bars represent standard deviations from the mean of the tests in (a-b).

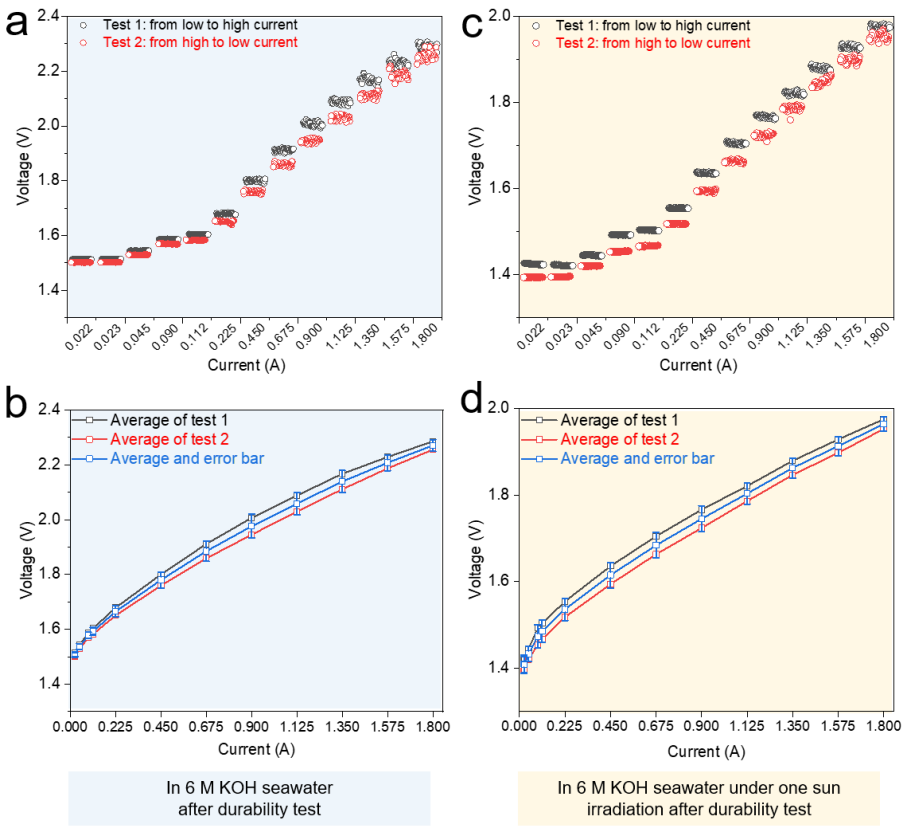

Supplementary Fig. S68. Overall seawater electrolysis performance by the NiMo-H_2||NiFe LDH pair (a-b) in 6 M KOH seawater and (c-d) in 6 M KOH seawater under simulated one sun irradiation after 192 h of durability testing at 0.45 A as shown in Fig. 5e. Error bars represent standard deviations from the mean of the tests in (a-b).

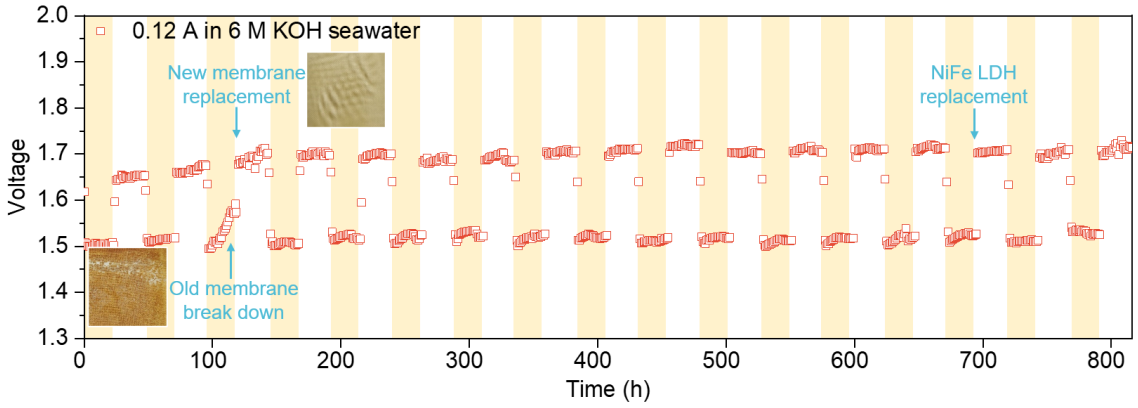

Supplementary Fig. S69. Chronopotentiometric curve for the NiMo-H_2||NiFe LDH pair at a constant current of 0.12 A in 6 M KOH seawater off and on cycles of illumination. Yellow regions represent durations of time when the light is on. Old membrane means the membrane has been used in other tests for a long time.

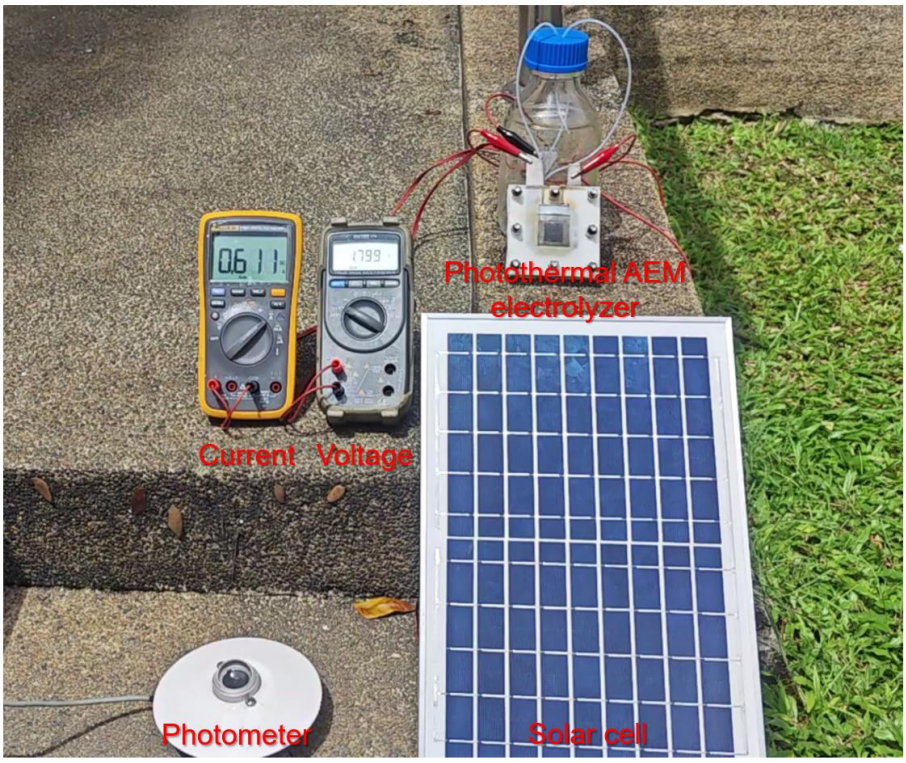

Supplementary Fig. S70. Outdoor green hydrogen production using the photothermal AEM electrolyzer with photothermal effect powered by a commercial solar cell.

Supplementary Note 1

The energy efficiency (η, %) of the water electrolysis is defined as the ratio of the theoretical voltage of water electrolysis (E_0) to the real cell voltage (V) measured at certain operating conditions.(*9*) It was calculated according to the following equations:(*10-12*)

$$\eta = E_0/V \quad (9)$$

$$E_0 = -\Delta G/nF \quad (10)$$

$$\Delta G = \Delta H - T\Delta S \quad (11)$$

in which ΔG is the change of Gibbs free energy, n is the number of electrons (2), F is the Faradaic constant (96485 C mol^{-1}), ΔH is the change of the enthalpy (−285.8 kJ mol^{-1}), T is the temperature, and ΔS is the change of entropy (−163.34 J K^{-1} mol^{-1}) during water electrolysis. At 25 °C and 1 atmosphere, the E_0 is calculated to be 1.229 V. To drive a current of 0.45 A, this photothermal AEM seawater electrolyzer composed of NiMo-H_2||NiFe LDH pair requires ~1.6 V (no *iR* compensation) under one sun irradiation, which is 0.2 V lower than the voltage required without light irradiation (~1.8 V). As a result, the energy efficiencies of the photothermal AEM electrolyzer with and without light irradiation were calculated to be ~76.8% and ~68.3%, respectively.

For the hydrogen production energy consumption (kWh/Nm^3) calculation, the volume of the H_2 gas production is calculated based on: $V_{H2} = Vm \times i \times t/(n \times F)$, where V_{H2} is the volume of the gas products (m^3), Vm is the molar volume, i is the current (A), t is the time (s, 3600 s for 1 h), n is the number of electrons (2), and F is the Faradaic constant (96485 C mol^{-1}) as above. The power is obtained by: P (W) = cell voltage (V) × current (I), the unit of which can further be convert to kW divided by 1000. For this photothermal AEM seawater electrolyzer, ~1.6 and ~1.8 V are required to reach current of 0.45 A with and without light irradiation. As a result, the energy consumption of this photothermal AEM seawater electrolyzer with and without light irradiation were calculated to be 3.83 and 4.31 kW·h/Nm^3, respectively.

Supplementary Table S1. Comparison of test conditions, HER catalytic activity, and durability performance between NiMo-H_2 and recently reported seawater electrolysis catalysts.

Catalyst	Test conditions	η (mV) @ 100 mA cm^{-2}	Tafel slope (mV dec^{-1})	*iR* drop	Scan rate (mV s^{-1})	Stability	Ref.
NiMo-H_2/NF	1 M KOH seawater with light irradiation in photothermal three-electrode and AEM electrolyzers	89	63.5	90%	1	500 mA cm^{-2} for 540 h in 6 M KOH seawater with light irradiation	This work
Pt-Ni@NiMoN/NF	1 M KOH seawater in three-electrode and AEM electrolyzers	47	30.6	100%	2	200 and 500 mA m^{-2} for 130 h in total in 1 M KOH seawater	(*13*)
Ni-MoN/CF	1 M KOH seawater in three- and two-electrode electrolyzers	66	36.8	Current Interrupt	1	500 mA cm^{-2} for 100 h in 1 M KOH seawater	(*14*)
Mo_2N/Ni_3Mo_3N/NF	1 M KOH seawater in three-electrode electrolyzer	74	57	N/A	1	10 mA cm^{-2} for 24 h in 1 M KOH seawater	(*15*)
NiMoN/NF	1 M KOH seawater in three- and two-electrode electrolyzers	82	N/A	Current Interrupt	5	100 and 500 mA cm^{-2} for 100 h each in 1 M KOH seawater for overall seawater electrolysis	(*16*)
CeO_2/α-MoC/β-Mo_2C/CC	1 M KOH seawater in three-electrode electrolyzer	~92	58.4	N/A	2	1000 mA cm^{-2} for 100 h in 1 M KOH seawater	(*17*)
Fe,P-$NiSe_2$/NFs	0.5 M KOH seawater in three-electrode and symmetric electrolyzers	~108	N/A	90%	5	410 mA cm^{-2} for 200 h in 1 M KOH seawater for overall seawater electrolysis	(*18*)
Co@RuCo/CP	1 M KOH seawater in three-electrode electrolyzer	~162	N/A	N/A	5	-300 mV for 50 h in 1 M KOH seawater	(*19*)
NiCo@C/MXene/CF	1 M KOH seawater in three-electrode and hybrid AEM electrolyzers	~170	N/A	N/A	1	-100 mV for 120 h in 1 M KOH seawater	(*20*)
NiP_2-FeP_2/Cu_{NW}/CF	1 M KOH + 0.6 M NaCl in three- and two-electrode electrolyzers	~175	N/A	85%	10	100 mA cm^{-2} for 275 h in 1 M KOH + 0.6 M NaCl for overall seawater electrolysis	(*21*)
NiTe-NiCoN/NF	1 M KOH seawater in three- and two-electrode electrolyzers	~177	N/A	85%	2	10, 20, 50, and 100 mA cm^{-2} for 10 h each in 1 M KOH seawater	(*22*)
CoO@C/MXene/NF	1 M NaOH seawater in three-electrode and hybrid AEM electrolyzers	~205	N/A	N/A	10	-470 mV for 80 h in 1 M KOH seawater	(*23*)
Ni_2P-Fe_2P/NF	1 M KOH seawater in three- and two-electrode and H-type electrolyzers	252	N/A	Current Interrupt	2	100/500 mA cm^{-2} for 36/22 h in 1 M KOH seawater	(*24*)
Ni_3N@C/NF	1 M KOH seawater in three- and two-electrode electrolyzers	314	N/A	N/A	2	100 and 500 mA cm^{-2} for 100 h each in 1 M KOH seawater for overall seawater electrolysis	(*25*)
Pt_{SA}-$Ni_{6.6}Fe_{0.4}P_3$/NF	4 M NaCl in three-electrode and hybrid AEM electrolyzers	-410	N/A	90%	5	100 mA cm^{-2} for 120 h in asymmetric electrolyzer (4 M NaCl-4 M NaOH)	(*26*)
Ru_2Co_1BO-350 powder	1 M KOH + 0.6 M NaCl in three- and two-electrode electrolyzers	~58	25.0	N/A	5	10 mA cm^{-2} for 20 h in 1 M KOH + 0.6 M NaCl	(*27*)
Ni-SN@C powder	1 M KOH seawater in three-electrode and hybrid AEM electrolyzers	~170	41	N/A	N/A	-25 mV for 40 h in 1 M KOH seawater	(*28*)
Ni-SA/NC powder	1 M KOH seawater in three-electrode electrolyzer	~280	82	N/A	5	-200 mV for 14 h in 1 M KOH seawater	(*29*)
Co-N,P-HCS powder	1 M KOH seawater in three-electrode and H-type electrolyzers	287	109.0	N/A	5	10 mA cm^{-2} for 100 h in 1 M KOH seawater	(*30*)

NF: nickel foam; CF: copper foam; CC: carbon cloth; NFs: $FeNiO_x$ nanoporous films; CP: carbon paper.

Supplementary Table S2. EXAFS data fitting results at the Ni K-edge of Ni foil, NiO and NiMo-H_2 samples.

Sample	Path	*CN*[a]	*R* (Å)[b]	σ^2 (Å^2)[c]	ΔE_0(eV)[d]	*R* factor
Ni foil	Ni-Ni	12.0*	2.479±0.003	0.0061	6.4±0.8	0.0040
NiO	Ni-O	6.2±0.9	2.076±0.011	0.0030	-2.1±1.4	0.0145
	Ni-Ni	14.1±0.7	2.952±0.008	0.0064		
NiMo-H_2	Ni-Ni	6.4±0.6	2.494±0.017	0.0045	-7.1±6.4	0.0142
	Ni-Mo	1.4±0.6	2.532±0.008	0.0045		

[a]*CN*, coordination number; [b]*R*, bond distance; [c]σ^2, Debye-Waller factors; [d]ΔE_0, inner potential correction to account for the difference in the inner potential between the sample and the reference compound; *R* factor indicates the goodness of the fit.

Supplementary Table S3. Comparison of AEM seawater electrolysis performance between the NiMo-H_2||NiFe LDH pair and recently reported catalysts.

Anode	Cathode	Voltage (V)	Current (A)	Area (cm^2)	*J* ($mA\ cm^{-2}$)	Electrolyte	Stability testing	Ref.
NiFe LDH/NF	NiMo-H_2/NF	~1.6	0.45	2.25	200	6 M KOH seawater	200 mA cm^{-2} for 192 h and ~53 mA cm^{-2} for >800 h each in self-designed photothermal AEM electrolyzer	This work
QDs@Ni_3N-MoN/Ti	QDs@Ni3N-MoN/Ti	1.12	0.25	0.25	1000	1 M KOH seawater + N_2H_4	500 and 2000 mA cm^{-2} for 300 h and 1000 mA cm^{-2} for 100 h each in commercial AEM electrolyzer	(*31*)
NiFe-WO_4 @WO_3/NF-1	Pt/Ti felt	1.6	0.8	4	200	Natural seawater	200 mA cm^{-2} for 250 h at 60°C in commercial electrolyzer	(*32*)
Ru-BO_x-OH-300	Ru-BO_x-OH-300	1.73	2	4	500	1 M KOH seawater	500 and 1000 mA cm^{-2} for 200 h each in commercial AEM electrolyzer	(*33*)
RuO_2	WC-RuV	~1.75	0.1	1	100	1 M KOH seawater	100 mA cm^{-2} for 22 h in commercial AEM electrolyzer	(*34*)
NiFe LDH/NF	NiS_x/NF	~1.75	24	120	200	6.9 M KOH seawater	200 mA cm^{-2} for 100 h at 80 °C in commercial electrolyzer	(*35*)
RuMoNi/NF	RuMoNi/NF	~1.8	1	2	500	1 M KOH seawater	500 mA cm^{-2} for 240 h at 20 ± 2 °C in commercial electrolyzer	(*36*)
NiFe LDH/NF	Pt-Ni_3N@V_2O_3 /NF	1.89	N/A	N/A	500	1 M KOH seawater	500 mA cm^{-2} for 100 h in commercial AEM electrolyzer	(*37*)
NiFeP@Ag/NF	Cu_2S@Ni/CF	1.95	0.4	1	400	1 M NaOH seawater	400 mA cm^{-2} for 1500 h in commercial electrolyzer	(*38*)
Ru-Ni_2P/Fe_2P /NF	Ru-Ni_2P/Fe_2P /NF	~2.0	N/A	N/A	500	1 M KOH seawater	500 mA cm^{-2} at 60 °C for 100 h in commercial AEM electrolyzer	(*39*)
NiFe-LDH/NF	MoO_x/$Co(OH)_2$/NF	2.25	N/A	N/A	500	1 M KOH seawater	N/A	(*40*)
CoFe-Ni_2P/Ni-felt	CoFe-Ni_2P/Ni-felt	2.25	1000	1	1000	6 M KOH seawater	1000 mA cm^{-2} for 350 h in commercial electrolyzer	(*41*)
(NiFe)C_2O_4/NF	Pt/C/NF	2.4	0.5	1	500	1 M NaOH seawater	500 mA cm^{-2} for 150 h in commercial PEM electrolyzer	(*42*)
$NiCoP_v$/NF	$NiCoP_v$/NF	2.43	N/A	N/A	500	1 M KOH seawater	500 mA cm^{-2} for 110 h in commercial AEM electrolyzer	(*43*)

Reference

1. S. Dresp, F. Dionigi, M. Klingenhof, P. Strasser, Direct Electrolytic Splitting of Seawater: Opportunities and Challenges. *ACS Energy Lett.* **4**, 933-942 (2019).
2. M. E. Assessment, *Ecosystems and human well-being: wetlands and water*. (World Resources Institute, 2005).
3. Y. Zhang *et al.*, Hetero-Interface Manipulation in MoO_x@Ru to Evoke Industrial Hydrogen Production Performance with Current Density of 4000 mA cm^{-2}. *Adv. Energy Mater.* **13**, (2023).
4. H. Chen *et al.*, Understanding the photothermal conversion efficiency of gold nanocrystals. *Small* **6**, 2272-2280 (2010).
5. J. Zhang *et al.*, Biocompatible D-A Semiconducting Polymer Nanoparticle with Light-Harvesting Unit for Highly Effective Photoacoustic Imaging Guided Photothermal Therapy. *Adv. Funct. Mater.* **27**, (2017).
6. H. Breitenborn *et al.*, Quantifying the photothermal conversion efficiency of plasmonic nanoparticles by means of terahertz radiation. *APL Photonics* **4**, (2019).
7. X. Cui *et al.*, Photothermal Nanomaterials: A Powerful Light-to-Heat Converter. *Chem. Rev.* **123**, 6891-6952 (2023).
8. J. Wang *et al.*, A Smart Photothermal Nanosystem with an Intrinsic Temperature-Control Mechanism for Thermostatic Treatment of Bacterial Infections. *Adv. Mater.* **34**, e2205653 (2022).
9. M. Chatenet *et al.*, Water electrolysis: from textbook knowledge to the latest scientific strategies and industrial developments. *Chem. Soc. Rev.* **51**, 4583-4762 (2022).
10. P. Chen, X. Hu, High-Efficiency Anion Exchange Membrane Water Electrolysis Employing Non-Noble Metal Catalysts. *Adv. Energy Mater.* **10**, (2020).
11. H. Koshikawa *et al.*, Single Nanometer-Sized NiFe-Layered Double Hydroxides as Anode Catalyst in Anion Exchange Membrane Water Electrolysis Cell with Energy Conversion Efficiency of 74.7% at 1.0 A cm^{-2}. *ACS Catal.* **10**, 1886-1893 (2020).
12. L. Wan, Z. Xu, Q. Xu, P. Wang, B. Wang, Overall design of novel 3D-ordered MEA with drastically enhanced mass transport for alkaline electrolyzers. *Energy Environ. Sci.* **15**, 1882-1892 (2022).
13. H. Hu *et al.*, An ultra-low Pt metal nitride electrocatalyst for sustainable seawater hydrogen production. *Energy Environ. Sci.* **16**, 4584-4592 (2023).
14. L. Wu *et al.*, Efficient Alkaline Water/Seawater Hydrogen Evolution by a Nanorod-Nanoparticle-Structured Ni-MoN Catalyst with Fast Water-Dissociation Kinetics. *Adv. Mater.* **34**, e2201774 (2022).
15. Z. Zhu *et al.*, High-Performance Alkaline Freshwater and Seawater Hydrogen Catalysis by Sword-Head Structured Mo_2N-Ni_3Mo_3N Tunable Interstitial Compound Electrocatalysts. *Adv. Funct. Mater.* **34**, (2023).
16. L. Yu *et al.*, Non-noble metal-nitride based electrocatalysts for high-performance alkaline seawater electrolysis. *Nat. Commun.* **10**, 5106 (2019).
17. M. Hu *et al.*, Coupling ceria with dual-phased molybdenum carbides for efficient and stable hydrogen evolution electrocatalysis at large-current-density in freshwater and seawater. *Appl Catal. B: Environ.* **317**, 121774 (2022).
18. J. Chang *et al.*, Dual-Doping and Synergism toward High-Performance Seawater Electrolysis. *Adv Mater.*. **33**, e2101425 (2021).

19. H. Huang *et al.*, Surface conversion derived core-shell nanostructures of Co particles@RuCo alloy for superior hydrogen evolution in alkali and seawater. *Appl Catal. B: Environ.* **315**, 121554 (2022).
20. F. Sun *et al.*, Energy-saving hydrogen production by chlorine-free hybrid seawater splitting coupling hydrazine degradation. *Nat. Commun.* **12**, (2021).
21. A. Kumar *et al.*, Modulating Interfacial Charge Density of NiP_2–FeP_2 via Coupling with Metallic Cu for Accelerating Alkaline Hydrogen Evolution. *ACS Energy Lett.* **6**, 354-363 (2021).
22. R. Li *et al.*, Synergistic interface engineering and structural optimization of non-noble metal telluride-nitride electrocatalysts for sustainably overall seawater electrolysis. *Appl Catal. B: Environ.* **318**, 121834 (2022).
23. L. Zhang, Z. Wang, J. Qiu, Energy-Saving Hydrogen Production by Seawater Electrolysis Coupling Sulfion Degradation. *Adv. Mater.* **34**, e2109321 (2022).
24. L. Wu *et al.*, Heterogeneous Bimetallic Phosphide Ni_2P-Fe_2P as an Efficient Bifunctional Catalyst for Water/Seawater Splitting. *Adv. Funct. Mater.* **31**, (2020).
25. Q. Wang *et al.*, Electrocatalytic Methane Oxidation Greatly Promoted by Chlorine Intermediates. *Angew. Chem. Int. Ed. Engl.* **60**, 17398-17403 (2021).
26. H. Shi *et al.*, A sodium-ion-conducted asymmetric electrolyzer to lower the operation voltage for direct seawater electrolysis. *Nat. Commun.* **14**, 3934 (2023).
27. L. W. Shen *et al.*, A RuCoBO Nanocomposite for Highly Efficient and Stable Electrocatalytic Seawater Splitting. *Nano Lett.* **23**, 1052-1060 (2023).
28. H. Jin *et al.*, Stable and Highly Efficient Hydrogen Evolution from Seawater Enabled by an Unsaturated Nickel Surface Nitride. *Adv. Mater.* **33**, e2007508 (2021).
29. W. Zang *et al.*, Efficient Hydrogen Evolution of Oxidized Ni-N_3 Defective Sites for Alkaline Freshwater and Seawater Electrolysis. *Adv. Mater.* **33**, e2003846 (2021).
30. X. Wang *et al.*, Asymmetric Co-N_3P_1 Trifunctional Catalyst with Tailored Electronic Structures Enabling Boosted Activities and Corrosion Resistance in an Uninterrupted Seawater Splitting System. *Adv. Mater.* **34**, e2204021 (2022).
31. H. Hu *et al.*, Optimizing the Dehydrogenation Kinetics of Metal Nitrides for Energy-Efficient Seawater Hydrogen Production at 2 A cm^{-2}. *Adv. Func. Mater.* **34**, (2024).
32. S. Zhao *et al.*, Lewis Acid Driving Asymmetric Interfacial Electron Distribution to Stabilize Active Species for Efficient Neutral Water Oxidation. *Adv. Mater.* **36**, e2308925 (2024).
33. J. Liang *et al.*, Electroreduction of alkaline/natural seawater: Self-cleaning Pt/carbon cathode and on-site co-synthesis of H_2 and Mg hydroxide nanoflakes. *Chem*, (2024).
34. Y. Zheng *et al.*, Oxophilic vanadium and deprotonated ruthenium atoms on tungsten carbide with accelerated intermediate migration for high-performance seawater hydrogen evolution. *Nano Energy* **127**, 109769 (2024).
35. H. Liu *et al.*, High-Performance Alkaline Seawater Electrolysis with Anomalous Chloride Promoted Oxygen Evolution Reaction. *Angew. Chem. Int. Ed. Engl.* **62**, e202311674 (2023).

36. X. Kang *et al.*, A corrosion-resistant RuMoNi catalyst for efficient and long-lasting seawater oxidation and anion exchange membrane electrolyzer. *Nat. Commun.* **14**, 3607 (2023).
37. H. Hu *et al.*, Efficient and durable seawater electrolysis with a V_2O_3-protected catalyst. *Sci. Adv.* **10**, eadn7012 (2024).
38. W. Xu *et al.*, Ag Nanoparticle-Induced Surface Chloride Immobilization Strategy Enables Stable Seawater Electrolysis. *Adv. Mater.* **36**, e2306062 (2024).
39. X. Li *et al.*, Vertically Staggered Porous Ni_2P/Fe_2P Nanosheets with Trace Ru Doping as Bifunctional Electrocatalyst for Alkaline Seawater Splitting. *Adv. Funct. Mater.* **34**, (2024).
40. J. Sun *et al.*, Reconstruction Co-O-Mo in amorphous-crystalline $MoO_x/Co(OH)_2$ interface for industry-level active and stable electrocatalytic seawater hydrogen evolution. *Nano Energy* **121**, 109246 (2024).
41. C. Huang *et al.*, Functional Bimetal Co-Modification for Boosting Large-Current-Density Seawater Electrolysis by Inhibiting Adsorption of Chloride Ions. *Adv. Energy Mater.* **13**, (2023).
42. Z. Li *et al.*, Carbon Oxyanion Self-Transformation on NiFe Oxalates Enables Long-Term Ampere-Level Current Density Seawater Oxidation. *Angew. Chem., Int. Ed. Engl.* **63**, (2023).
43. L. Guo *et al.*, Phosphorus Defect Mediated Electron Redistribution to Boost Anion Exchange Membrane-Based Alkaline Seawater Electrolysis. *Adv. Energy Mater.* **14**, (2024).